

The NuSTAR view of five changing-look active galactic nuclei

Bing Lyu ,¹[★] Zhen Yan ,² Xue-bing Wu ,^{1,3} Qingwen Wu,⁴ Wenfei Yu ,² Hao Liu ,⁵

¹*Kavli Institute for Astronomy and Astrophysics, Peking University, Beijing 100871, People's Republic of China*

²*Shanghai Astronomical Observatory, Chinese Academy of Sciences, 80 Nandan Road, Shanghai, 200030, People's Republic of China*

³*Department of Astronomy, School of Physics, Peking University, Beijing, 100871, People's Republic of China*

⁴*Department of Astronomy, School of Physics, Huazhong University of Science and Technology, 1037 Luoyu Road, Wuhan, 430074, People's Republic of China*

⁵*University of Science and Technology of China, No.96, JinZhai Road Baohe District, Hefei, Anhui, 230026, People's Republic of China*

17 January 2025

ABSTRACT

Changing-look active galactic nuclei (CLAGNs) are known to change their spectral type between 1 and 2 (changing-state) or change their absorption between Compton-thick and Compton-thin (changing-obscuration) on timescales of years or less. The physical mechanism and possible connection between the two types of CLAGNs are still unclear. We explore the evolution of the broadband X-ray spectra from Nuclear Spectroscopic Telescope Array (*NuSTAR*) and column density in five CLAGNs with moderate inclination viewing angles, which have shown significant variations of both optical types and X-ray absorption. Based on a phenomenological and two clumpy torus models, we find that the X-ray photon index (Γ) and the Eddington-scaled X-ray 2 – 10 keV luminosity (L_X/L_{Edd}) are positively correlated for the five sources, which are similar to other bright AGNs and optical CLAGNs at type 1 phase. We find a significant negative correlation between $\log N_{\text{H,los}}$ and $\log L_X/L_{\text{Edd}}$ except for ESO 362-G18. Similar to changing-state AGNs, changing-obscuration AGNs may be also triggered by the evolution of the accretion disc. Our results support the disc wind scenario, where the disc wind proportional to the accretion rate and formed at moderate inclination angles would push the obscuration material further away and decrease the column density from the line of sight observed in the changing-look AGNs.

Key words: X-rays: galaxies – galaxies: nuclei – galaxies:Seyfert – accretion

1 INTRODUCTION

An Active Galactic Nucleus (AGN) is a compact region at the center of a galaxy, which is powered by the material accreting onto a supermassive black hole (SMBH, e.g., Ho 2008). AGNs are empirically divided into type 1 AGNs with both broad emission lines (e.g., FWHM $\gtrsim 1000$ km/s) and narrow emission lines (FWHM $\lesssim 500$ km/s) and type 2 AGNs with only narrow emission lines. The sub-classes (e.g., Seyfert 1.5, 1.8, and 1.9) are further defined with the declines of the broad H β emission lines relative to narrow [O III] lines (Osterbrock & Koski 1976; Osterbrock 1981). The broad H β lines are undetectable and very weak in type 1.9 and type 1.8 AGN. The broad H α and H β lines are comparable in type 1.5 AGN. The difference between the two types of AGNs is attributed to the different inclination angles with respect to the line of sight in the so-called unified model of AGN (e.g., Antonucci 1993; Netzer 2015). In this scenario, the broad emission lines come from the broad line region (BLR) at the sub-pc scale and the narrow emission lines come from the narrow line region (NLR) at the kpc scale. Type 1 AGNs are face-on viewed with the

broad emission lines visible to us, while type 2 AGNs are edge-on and the broad emission lines are obscured by the surrounding dusty torus. Their intrinsic properties are considered to be the same and their optical classification and absorption from torus should not change in such a short timescale of years or even months. However, two kinds of CLAGNs, optical (appearance/disappearance of broad emission lines) and X-ray CLAGNs (switch between Compton thin & Compton-thick state) are observed in recent years, which propose challenges to the traditional unified model of AGN.

The optical changing-look AGNs are also referred to as changing-state AGN, (CS-AGN; e.g. Ricci & Trakhtenbrot 2023), where their broad emission lines appear or disappear within several months to years (e.g., Denney et al. 2014; Shappee et al. 2014; LaMassa et al. 2015; Yang et al. 2018; Wang et al. 2019; Trakhtenbrot et al. 2019; Raimundo et al. 2019; Katebi et al. 2019; Wang et al. 2020; Yang et al. 2023). The traditional explanation is due to the obscuring clouds moving into the line of sight and block the broad emission lines (e.g. Risaliti et al. 2009). However, this explanation can only be applied to a few sources (e.g. Marin et al. 2013; Ag $\acute{\text{s}}$ -Gonz $\acute{\text{a}}$ lez et al. 2014; Rivers et al. 2015; Turner et al. 2018; Zeltyn et al. 2022). Besides, this scenario is inconsistent with the low N_{H} and significant mid-infrared (MIR) variability found for

* E-mail:lyubing@pku.edu.cn

2 Bing Lyu et al.

most of the optical CLAGNs (e.g. Sheng et al. 2017; Noda & Done 2018). Another explanation is related to the change of the accretion rate (e.g. Jana et al. 2024; Zeltyn et al. 2024; Panda & Śniegowska 2024). Those optical CLAGNs with suppression/enhancement of the blue continuum and disappearance/appearance of the broad emission lines are usually accompanied by the accretion-rate driven multi-wavelength and rapid variability. On the one hand, as the accretion rate decreases, it is hard to sustain the BLR, and AGN would follow a sequence from type 1, 1.2/1.5, 1.8/1.9, to 2 in a disc-wind BLR model (e.g. Elitzur et al. 2014). On the other hand, the inner part of standard Shakura-Sunyaev thin disc (SSD; Shakura & Sunyaev 1973) could be truncated by a radiatively inefficient accretion flow (RIAF) (e.g., Ho 2008; Yuan & Narayan 2014) when the accretion rate is lower than a critical value and the disc provides deficient ionizing photons to excite the gas in the BLR (e.g. Noda & Done 2018; Guolo et al. 2021). The 6.4 keV Fe-K α line is a ubiquitous feature in AGNs' X-ray spectra, which could be a probe of the BLR or the torus materials (e.g., Noda et al. 2022). The dust sublimation radius serves as an outer envelope of the Fe-K α line emitting region (e.g., Gandhi et al. 2015), which is confirmed in most AGNs with the narrow Fe-K α regions smaller than dusty sublimation radius (Andonie et al. 2022). The narrow Fe-K α line emitting region from the reverberation mapping for NGC 3516 at type 2 phase is consistent with the location of BLR at type 1 phase and is significantly smaller than the dusty torus radius (Noda et al. 2022), which suggests the BLR materials remain during the type 2 phase and confirms the latter scenario.

X-ray CLAGNs are originally referred to as AGNs that show variable X-ray spectra switching from/to Compton-thick AGNs ($N_{\text{H}} \gtrsim 10^{24} \text{ cm}^{-2}$) to/from Compton-thin AGNs ($N_{\text{H}} < 10^{24} \text{ cm}^{-2}$) (e.g., Matt et al. 2003; Puccetti et al. 2007; Bianchi et al. 2009; Agís-González et al. 2014; Rivers et al. 2015; Ricci et al. 2016; Marchesi et al. 2022). The line of sight column density (N_{H}), which reflects the properties of the torus, can be determined by the X-ray spectral fitting since the obscuring materials significantly absorb the emission below soft X-ray (e.g. $< 10 \text{ keV}$) band due to the internal dust extinction (Matt 2002). Those AGNs with a rapid and extreme variation of N_{H} (e.g., variation larger than one order of magnitude in timescales of years or months) could be also considered as X-ray CLAGNs or changing-obscuration AGN (CO-AGN; see a recent review in Ricci & Trakhtenbrot 2023). For the changing-obscuration AGNs, the rapid variation of the column density can be attributed to the motion of obscuring clouds (Ricci et al. 2016) or the clumpy torus (Risaliti et al. 2009). Otherwise, it might also be related to the change of intrinsic accretion rate, e.g., the change in the ionization state of the obscuring material (e.g. Yaqoob et al. 1989; Neustadt et al. 2023; Ricci & Trakhtenbrot 2023), the sublimation of dust in the clouds near the BLR (e.g. Jana et al. 2021), or the disc wind associated with the variation of the intrinsic AGN luminosity (e.g. Ricci et al. 2017; Mondal et al. 2022).

The number of CLAGNs is growing quickly but the total number is still limited ($\lesssim 300$ for optical CLAGNs, e.g., MacLeod et al. 2019; Sheng et al. 2020; Potts & Villforth 2021; Senarath et al. 2021; Jin et al. 2022 and ~ 23 for X-ray CLAGNs, e.g., Lyu et al. 2022; Marchesi et al. 2022, and references therein). Less than 13 CLAGNs show repeating behavior of appearance/disappearance of broad emission lines (e.g. Śniegowska et al. 2020; Wang et al. 2022). CLAGNs with both the appearance/disappearance of broad emission line and the significant variation of N_{H} are much rarer (Lyu et al. 2022). The mechanism for the rapid variation of column density and the geometry of the torus for changing-obscuration AGNs are under debate. The possible association and discrepancy

between the two types of changing-look phenomena are still unclear. The broadband X-ray spectral evolution of CLAGNs with both the variation of broad emission line and N_{H} might help us to explore these issues. The broadband X-ray spectra are crucial in determining the absorption and torus properties. In this work, we analyzed the Nuclear Spectroscopic Telescope Array (*NuSTAR*; Harrison et al. 2013) spectra of five changing-look AGNs, which experienced both the rapid variation of the broad emission lines and the column density. In section 2, we describe the basic information of the sample. In section 3, we present the data reduction and analysis. We simply discuss the possible explanation of the result in section 4 and section 5 and summarize in section 6. Throughout this work, we adopt a flat Λ -CDM cosmological model with $H_0=70 \text{ km s}^{-1} \text{ Mpc}^{-1}$, $\Omega_m=0.27$, and $\Omega_{\Lambda}=0.73$.

2 SAMPLE

The sample we collect meets the following criteria: (1) has experienced the appearance/disappearance of broad Balmer emission lines (2) extreme significant variation of the hydrogen column density in the obscured state (i.e., $\log(\Delta(N_{\text{H}})) > 1$ and $\log(N_{\text{H}}/\text{cm}^{-2}) > 22$) (3) at least one *NuSTAR* observation. Thus, ESO 362-G18, NGC 1365, NGC 4151, NGC 5548, and NGC 7582 are selected in our sample (e.g., Puccetti et al. 2007; Bianchi et al. 2009; Agís-González et al. 2014; Braito et al. 2014; Agís-González et al. 2018; Marin et al. 2019; Lyu et al. 2022; Temple et al. 2023). 3C 390.3 as a radio-loud galaxy is ruled out to avoid the jet effects. All of the sample are nearby and extremely variable Seyfert galaxies, thus abundant multi-epoch observations have been carried out to capture the changing-look events. All of them have a moderate disc inclination angle, and a relatively small BH mass (i.e., $\log(M_{\text{BH}}/M_{\odot})$ between 6.65 and 7.74). For further study of the mechanism of changing-state and changing-obscuration phenomena, we take these five sources as a sample. The detailed information of the sample (i.e., ESO 362-G18, Agís-González et al. 2014, 2018; NGC 1365, Braito et al. 2014; Temple et al. 2023; NGC 4151, Puccetti et al. 2007; Marin et al. 2019; NGC 5548, Dehghanian et al. 2019; Kaastra et al. 2014; NGC 7582, Bianchi et al. 2009; Marin et al. 2019) is listed in Table 1 and presented in the appendix.

3 DATA REDUCTION AND ANALYSIS

The *NuSTAR* FPMA/FPMB data were retrieved from *NuSTAR* Archive¹ and reduced through the nupipeline task of the nusardas v2.1.2 package with the CALDB v20220316. The source and background spectra were extracted from a 90'' radius circle at the center of the source and a blank region, respectively. Each spectrum is grouped by a minimum of 30 counts per bin through the grppha command. The observational information of *NuSTAR* data is listed in Table 2. We also reduced the soft X-ray data from *XMM-Newton*/PN and *Swift*/XRT for part of *NuSTAR* observations (see Table 2). The *XMM-Newton*/PN data were reduced through Science Analysis Software (SAS, version 19.1.0). The source and background spectra were extracted through epproc from a circular region with a 40 arcsec radius that includes and excludes the source, respectively. The *Swift*/XRT data in the photon-counting

¹ https://heasarc.gsfc.nasa.gov/docs/nustar/archive/nustar_archive.html

Table 1. Basic information of five CLAGNs. The table lists source name, redshift, the corresponding luminosity distance, the Galactic absorption ($N_{\text{HI,Gal}}$) from [Kalberla et al. \(2005\)](#) adopted for X-ray spectral fitting, BH mass, inclination angle, and references.

Name	Ref	Redshift	Luminosity distance Mpc	$N_{\text{HI,Gal}}$ [10^{20} cm^{-2}]	$\log(M_{\text{BH}}/M_{\odot})$	Ref	disc inclination angle [deg]	Ref
ESO 362-G18	(1,2)	0.0124	53.8	1.8	7.65	(1)	$\sim 53 \pm 5$	(1)
NGC 1365	(3,4)	0.0055	23.5	1.3	6.65	(10)	$\sim 57^{+3}_{-2}$	(14)
NGC 4151	(5,6)	0.0033	14.3	2.3	7.6	(11)	$\sim 58^{+8}_{-10}$	(15)
NGC 5548	(7,8)	0.0172	74.6	1.6	7.7	(12)	$\sim 39^{+12}_{-11}$	(16)
NGC 7582	(9,6)	0.0053	22.6	1.3	7.74	(13)	~ 68	(17)

References. (1) [Agís-González et al. \(2014\)](#) (2) [Agís-González et al. \(2018\)](#) (3) [Braito et al. \(2014\)](#) (4) [Temple et al. \(2023\)](#) (5) [Puccetti et al. \(2007\)](#) (6) [Marin et al. \(2019\)](#) (7) [Dehghanian et al. \(2019\)](#) (8) [Kaastra et al. \(2014\)](#) (9) [Bianchi et al. \(2009\)](#) (10) [Onori et al. \(2017\)](#) (11) [Li et al. \(2022\)](#) (12) [Bentz & Katz \(2015\)](#) (13) [Wold et al. \(2006\)](#) (14) [Walton et al. \(2010\)](#) (15) [Bentz et al. \(2022\)](#) (16) [Pancoast et al. \(2014\)](#) (17) [Paturel et al. \(2003\)](#)

mode were reduced by `XRTPIPELINE`. We extracted the spectra following the methods in [Lyu et al. \(2021\)](#).

There is only one *NuSTAR* observation for ESO 362-G18, which had low column density based on the Warm Corona and Relativistic Reflection models when combining the *XMM-Newton* data (e.g., [Zhong & Wang 2022](#)). For NGC 1365, the three *NuSTAR* spectra (ObsID 60002046005, 60002046007, and 60002046009) showed strong absorption iron lines around 6.7 keV and 7.0 keV during 2012 and 2013 ([Liu et al. 2021](#)). For these spectra, we adopted the results from [Liu et al. \(2021\)](#). For NGC7582, [Lefkir et al. \(2023\)](#) performed a detailed time-resolved spectral analysis for the *NuSTAR* data in 2016 (ObsID 60201003002) based on a phenomenological model (xillver). The *NuSTAR* spectra are fitted in the 3–60 keV energy range with `xspec` v12.12.1 ([Arnaud 1996](#)) with the χ^2 statistic. First, we fix the inclination angle to the values reported in [Table 1](#).

3.1 pexrav

We start the spectral fitting with a simple absorbed powerlaw model with exponential cut-off `CONST * PHABS1 * (ZPHABS2*CABS*ZCUTOFFPL1)`, where the `CONST` component represents the cross-calibration constants between different instruments, `PHABS1` represents the Galactic absorption, the additional `ZPHABS2` and `CABS` represent the line-of-sight absorption to account for the obscuration of the AGN. This simple model provides acceptable fits for ESO 362-G18 and the column density estimated is the same as that from the data constrained by only the *NuSTAR* data. The fitting is not quite acceptable for the other sources, so we add the re-processed emission component modeled with `pexrav` ([Magdziarz & Zdziarski 1995](#)) which represents the reprocessed X-ray emission from a cold, neutral, and semi-infinite slab. For ESO 362-G18, the added reflection component makes little difference to the fitting results. The iron abundance is set to one. We add a Gaussian line representing the Fe K α line. When the line width is not constrained, we fix it to 50 eV (e.g., [Jana et al. 2022](#)). When the cut-off energy of the primary component in `pexrav` is not well constrained, we fix it to 200 keV (e.g., [Liu et al. 2022](#)) or link to the value of the observation with the longest exposure. For sources with high column densities, a scattered component is also usually observed. We then include one cutoff powerlaw component (`CONST2*ZCUTOFFPL2`) representing the scattered component, where `CONST2` represents the scattering fraction (f_s). The X-ray photon index, cut-off energy, and normalization of the scattered component are linked to the primary continuum. The final model configuration used in `xspec` is as follows,

const1 * phabs1 * (zphabs2 * cabs * zcutoffpl1

$$+zgauss + pexrav + const2 * zcutoffpl2).$$
 (1)

The simple `pexrav` model provides good descriptions of the *NuSTAR* data. The parameters of the fitting results are listed in [Table B1](#). The intrinsic X-ray flux is calculated by `cflux` component. To study the spectral evolution and the variability of N_{H} , the parameters we are mainly concerned about are the X-ray photon index (Γ), the column density of line-of-sight ($N_{\text{H,los}}$), and the X-ray flux at 2–10 keV. The intrinsic Eddington-scaled X-ray luminosity is estimated through error propagation based on the BH mass and the distance in [Table 1](#). The uncertainties of all spectral parameters are reported at the 90 percent confidence level if not otherwise specified. We also include the (quasi)-simultaneous *XMM-Newton* or *Swift*/XRT data for part of *NuSTAR* observations (see [Table 2](#)) to better constrain the column density.

The extreme variability of column density might be explained by the clumpy torus or the motion of obscuration material. We further consider two popular and physically motivated clumpy torus models (`XCLUMPY` and `UXCLUMPY`) to constrain the column density for the five CLAGNs. The best-fitted unfolded spectra with the `pexrav` model and two clumpy torus models are available in the appendix files.

3.2 XCLUMPY

As the changing look might be caused by the clumpy torus, we then test the widely used clumpy torus model `xclumpy`² ([Tanimoto et al. 2019](#)). The `xclumpy` model assumes a powerlaw distribution of clumps of the torus in the radial direction and a normal distribution in the elevation direction. The `xclumpy` model has two components, `XCLUMPY_R` and `XCLUMPY_L`, which represent the re-processed and line emission, respectively. The model configuration used in `xspec` is as follows,

$$\begin{aligned} \text{const1} * \text{phabs1} * (\text{zphabs2} * \text{cabs} * \text{zcutoffpl1} \\ + \text{xclumpy_R} + \text{const2} * \text{xclumpy_L} \\ + \text{const3} * \text{zcutoffpl2}). \end{aligned}$$
 (2)

The equatorial column density, the inclination angle, and the torus angular width (σ_{tor}) are free parameters, and the line-of-sight column density is linked with the above parameters in `xclumpy` model

² <https://github.com/AtsushiTanimoto/XClumpy>

Table 2. The *NuSTAR* observations of five CLAGNs studied in this work. The table lists source name, *NuSTAR* observational ID, date, and exposure time. Observations with at least an exposure time of 1 ks are adopted. We also include (quasi)-simultaneous soft X-ray data from *XMM-Newton* and *Swift/XRT* for part of *NuSTAR* observations.

Name	ObsID	MJD	Date	Exposure (ks)
ESO 362-G18	60201046002	57655.8	2016-9-24	101.91
	790810101 (<i>XMM-Newton</i>)		2016-9-24	
NGC 1365	60002046002	56133.9	2012-7-25	36.26
	692840201 (<i>XMM-Newton</i>)		2012-7-25	
	60002046003	56134.7	2012-7-26	40.59
	35458003(<i>Swift/XRT</i>)		2012-7-26	
	60702058002	59320.9	2021-4-16	56.30
	96123002(<i>Swift/XRT</i>)		2021-4-19	
	60702058004	59326.8	2021-4-22	38.05
	89213003(<i>Swift/XRT</i>)		2021-4-22	
	60702058006	59333.3	2021-4-29	11.85
	60702058008	59336.0	2021-5-2	44.66
NGC 4151	60702058010	59340.5	2021-5-6	41.48
	60702058012	59342.7	2021-5-8	50.70
	60001111002	56243.3	2012-11-12	21.86
	80073001(<i>Swift/XRT</i>)		2012-11-12	
	60001111003	56243.8	2012-11-12	57.03
	60001111005	56245.3	2012-11-14	61.53
	60502017002	58688.3	2019-7-24	31.74
	60502017004	58799.4	2019-11-12	43.74
	88889001(<i>Swift/XRT</i>)		2019-11-12	
	60502017006	58841.5	2019-12-24	32.40
NGC 5548	60502017008	58858.3	2020-1-10	30.59
	88889004(<i>Swift/XRT</i>)		2020-1-10	
	60502017010	58867.5	2020-1-19	29.72
	60502017012	58871.3	2020-1-23	28.86
	88889005(<i>Swift/XRT</i>)		2020-1-23	
	60002044002	56484.4	2013-7-11	24.10
	91744028(<i>Swift/XRT</i>)		2013-7-11	
	60002044003	56485.0	2013-7-12	27.27
	91711077(<i>Swift/XRT</i>)		2013-7-12	
	60002044005	56496.6	2013-7-23	49.52
NGC 7582	91744040(<i>Swift/XRT</i>)		2013-7-23	
	60002044006	56545.9	2013-9-10	51.46
	91711139(<i>Swift/XRT</i>)		2013-9-10	
	60002044008	56646.4	2013-12-20	50.10
	80131001(<i>Swift/XRT</i>)		2013-12-21	
	90701601002	59240.3	2021-1-26	38.72
	95671036(<i>Swift/XRT</i>)		2021-1-23	
	60061318002	56170.7	2012-8-31	16.46
	32534001(<i>Swift/XRT</i>)		2012-9-1	
	60061318004	56184.7	2012-9-14	14.56
782720301 (<i>XMM-Newton</i>)	60201003002	57506.2	2016-4-28	48.49
			2016-4-28	

as follows (Tanimoto et al. 2019),

$$N_{\mathrm{H}}^{\mathrm{los}} = N_{\mathrm{H}}^{\mathrm{Eq}} \left[\exp \left(\frac{(i - \pi/2)^2}{\sigma_{\mathrm{Tor}}^2} \right) \right]. \quad (3)$$

The photon index, cutoff energy, normalization of the primary component, the reprocessed and line component are linked together, and the other parameters of the reprocessed and line component are linked. The `xclumpy` model considers a fixed cut-off energy at $E_{\mathrm{cut}} = 370$ keV. The `const2` and `const3` represent the relative normalization (A_{L}) of the line emission and the scattering fraction (f_{s}). We also try to constrain the inclination angles from the line of sight

by setting it as a free parameter and jointly fitting the spectra. The parameters of the fitting results are presented in Table B2.

3.3 UXCLUMPY

Another clumpy torus model UXCLUMPY³ (Buchner et al. 2019) is also tested. The UXCLUMPY model assumes an axisymmetric and

³ <https://github.com/JohannesBuchner/xars/blob/master/doc/uxclumpy.rst>

clumpy distribution of obscuring material. The number N of clouds between the observer and the central AGN is

$$N = N_0 \times \exp\left(-\left(\frac{\beta}{\text{TOR}\sigma}\right)^2\right), \quad (4)$$

where N_0 is the number of clouds on the equatorial plane that remains constant, β is the inclination angle toward the torus pole, and $\text{TOR}\sigma$ is the obscuring material angular width, which represents the torus scale height. Besides, the UXCLUMPY model includes an inner Compton-thick ring of clouds with covering factor CTK (CTKcov) as a free parameter, and the column densities of these clouds are $\log N_{\text{H}} = 25 \pm 0.5$. The column density of line-of-sight could be variable while the obscurer geometry keeps self-consistent. The model configuration used in xspec is as follows,

$$\text{const1} * \text{phabs} * (\text{uxclumpy_cutoff.fits} + f_s * \text{uxclumpy_cutoff_omni.fits}), \quad (5)$$

where UXCLUMPY models the transmitted and the reflected component (including the fluorescent lines), and uxclumpy_omni models the so-called warm mirror emission (scattered emission). The scatter fraction is limited between 1e-5 and 0.1. The parameters of the UXCLUMPY and uxclumpy_omni were linked. We froze the cutoff energy at 370 keV to be consistent with xclumpy. We set CTKcov = 0.4 at first and then let CTKcov as a free parameter and refit the spectra. Similarly, We also thaw the parameter of the inclination angle and refit the spectra. The parameters of the fitting results are presented in Table B3.

4 RESULTS

The X-ray spectral photon indices are between ~ 1.4 and ~ 2.0 , which are harder than other typical bright AGNs. The Eddington-scaled X-ray luminosity $\log L_{2-10\text{keV}}/L_{\text{Edd}}$ range between ~ -4.5 and ~ -2.5 . Adopting the bolometric correction factors from Netzer (2019), the Eddington ratio ($\lambda = \log L_{\text{bol}}/L_{\text{Edd}}$) range between ~ -3.5 and ~ -1.0 .

4.1 Correlations

To study the possible mechanism of the variability of the column density (i.e., obscuration effects or intrinsic accretion variation), we present the correlation between Γ , $\log N_{\text{H},\text{los}}$, and $\log L_{\text{X}}/L_{\text{Edd}}$ based on the pexrav model in Figure 1. We use the linregress⁴ in the scipy.stats Python module to perform linear regression. The slope and intercept of the linear function, Pearson's correlation coefficient (R -value), and p -values are reported in Table 4.1.

There is only one *NuSTAR* observation of ESO 362-G18 with low column density, which significantly deviates from the best-fit line for the $\log N_{\text{H},\text{los}}-\log L_{\text{X}}/L_{\text{Edd}}$ correlation. Then we exclude ESO 362-G18 during the linear fitting. We find a significant negative $\log N_{\text{H},\text{los}}-\log L_{\text{X}}/L_{\text{Edd}}$ correlation (slope = -0.75 ± 0.16), where the R -value is -0.67 ± 0.07 ($p = 6.7 \times 10^{-5}$). For NGC 1365, we combine three *NuSTAR* observations, which show strong absorption iron lines (Liu et al. 2021). For individual sources, the $\log N_{\text{H},\text{los}}$ is also roughly anti-correlated with $\log L_{\text{X}}/L_{\text{Edd}}$. For NGC 1365, there is a steeper correlation (slope = -1.23) with $R = -0.85 \pm 0.06$ ($p = 9.3 \times 10^{-4}$). For NGC 7582, there are only three *NuSTAR* observations. We adopt the results from Lefkir et al. (2023), which

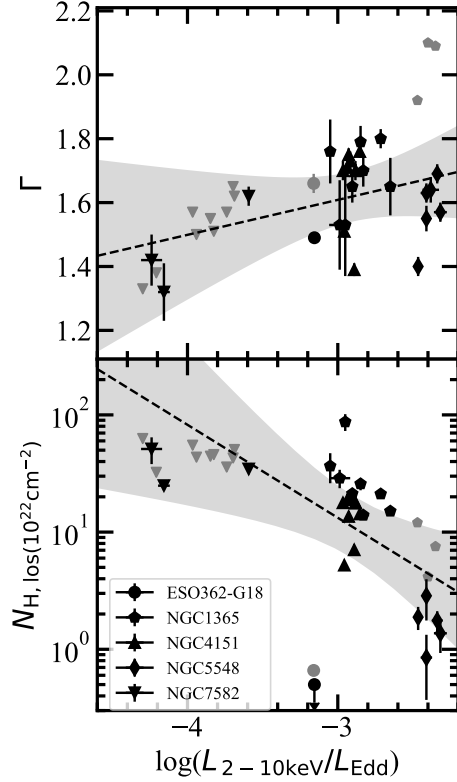


Figure 1. Relations between Γ , $\log N_{\text{H},\text{los}}$, and $\log L_{\text{X}}/L_{\text{Edd}}$ based on pexrav model. The circle, pentagon, up-triangle, and down-triangle represent ESO 362-G18, NGC 1365, NGC 4151, and NGC 7582. The dashed line represents the best-fit line with a 3σ confidence interval within the shaded region for all sources. Here, ESO 362-G18 is an obvious outlier in the $\log N_{\text{H},\text{los}}-\log L_{\text{X}}/L_{\text{Edd}}$ correlation. The grey data points are from the literature for comparison (see Table B4).

performs a detailed time-resolved spectral analysis of the *NuSTAR* observations in 2016 based on a phenomenological reflection model (see Table B4). NGC 7582 showed less variability of column density with a slope of -0.07 ± 0.15 .

There is a positive correlation between Γ and $\log L_{\text{X}}/L_{\text{Edd}}$ (slope = 0.11 ± 0.05) for the whole sample, where the R -value is 0.39 ($p=4.7 \times 10^{-2}$). The positive correlation between Γ and $\log L_{\text{X}}/L_{\text{Edd}}$ also holds for NGC 1365, NGC 5548, and NGC 7582 with slopes of 0.68 ± 0.14 , 1.29 ± 0.96 , and 0.46 ± 0.06 , respectively. For NGC 4151, the significance ($R=0.11 \pm 0.21$) is not so strong due to its less variability in X-ray luminosity.

For further study and comparison, the correlations between Γ , $\log N_{\text{H},\text{los}}$, and $\log L_{\text{X}}/L_{\text{Edd}}$ based on two clumpy torus models are presented in Figure 2. The positive correlation between Γ and $\log L_{\text{X}}/L_{\text{Edd}}$ for the five sources and the negative correlation between $\log N_{\text{H},\text{los}}$ and $\log L_{\text{X}}/L_{\text{Edd}}$ excluding ESO 362-G18 are further confirmed. The slopes of the $\Gamma-\log L_{\text{X}}/L_{\text{Edd}}$ correlation and Pearson's correlation coefficients (R -value), and p -values are 0.23 ± 0.03 , 0.84 ± 0.04 , and $4.1\text{e-}8$ for the XCLUMPY model and 0.21 ± 0.02 , 0.89 ± 0.03 , and $3.2\text{e-}10$ for the UXCLUMPY model, respectively. The slopes of the $\log N_{\text{H},\text{los}}-\log L_{\text{X}}/L_{\text{Edd}}$ correlation and Pearson's correlation coefficients (R -value), and p -values are -0.56 ± 0.11 , -0.71 ± 0.07 , and $5.2\text{e-}05$ for the XCLUMPY model and -0.61 ± 0.08 , -0.85 ± 0.04 , and $3.9\text{e-}8$ for the UXCLUMPY model, respectively. We also present the correlations between Γ , $\log N_{\text{H},\text{los}}$, and $\log L_{\text{bol}}/L_{\text{Edd}}$ for comparison in Figure 3.

⁴ <https://docs.scipy.org/doc/scipy/reference/generated/scipy.stats.linregress.html>

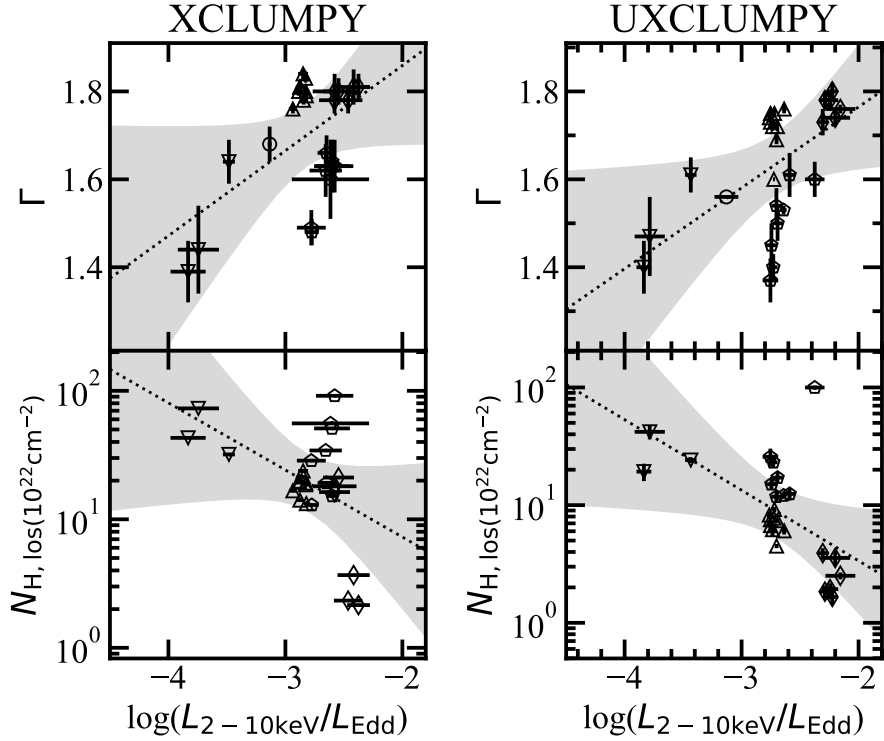


Figure 2. Relations between Γ , $\log N_{\text{H}, \text{los}}$, and $\log L_{\text{X}}/L_{\text{Edd}}$ for two clumpy torus models.

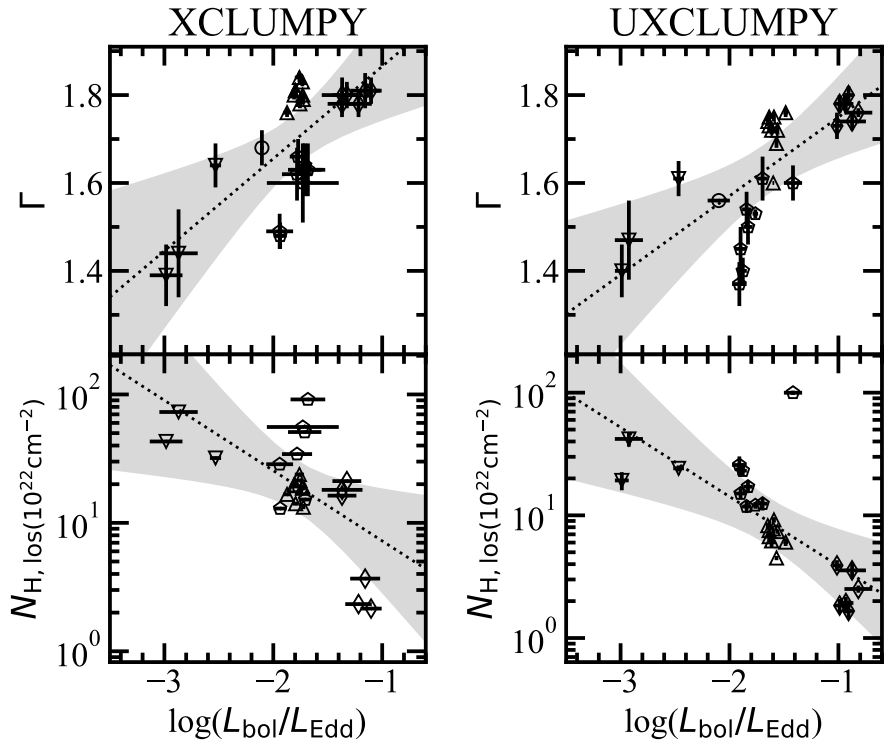
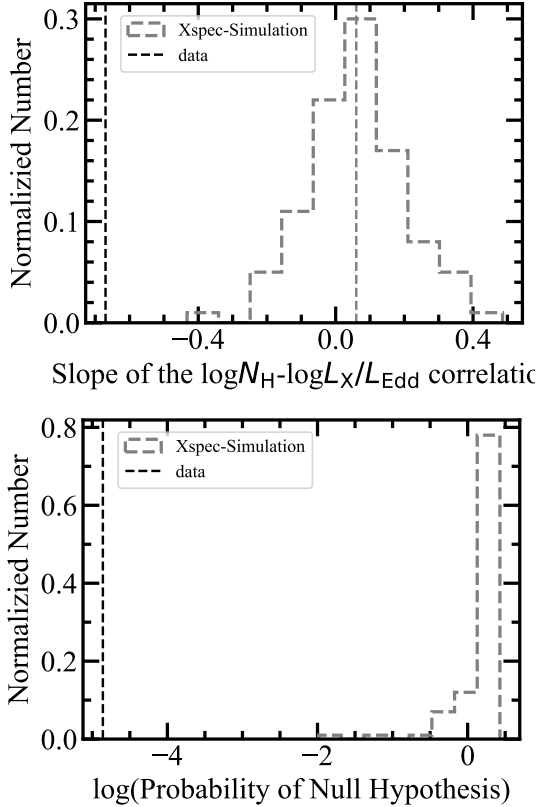


Figure 3. Relations between Γ , $\log N_{\text{H}, \text{los}}$, and $\log L_{\text{bol}}/L_{\text{Edd}}$ for two clumpy torus models. Bolometric correction factors are adopted from [Netzer \(2019\)](#).

Table 3. Correlations for Γ - $\log L_X/L_{\text{Edd}}$ and $\log N_{\text{H},\text{los}}$ - $\log L_X/L_{\text{Edd}}$ based on the pexrav model.

Sample	slope	intercept	R -value	P -value
Γ - $\log L_X/L_{\text{Edd}}$				
All sample	0.11 ± 0.05	1.94 ± 0.15	0.39 ± 0.11	$4.7\text{-}02$
ESO 362-G18 excluded	0.18 ± 0.06	2.19 ± 0.19	0.48 ± 0.10	$8.5\text{-}03$
NGC 1365	0.68 ± 0.14	3.65 ± 0.38	0.85 ± 0.05	$8.0\text{-}04$
NGC 4151	0.35 ± 1.24	2.68 ± 3.63	0.11 ± 0.22	$7.9\text{-}01$
NGC 5548	1.29 ± 0.69	4.65 ± 1.65	0.68 ± 0.15	$1.4\text{-}01$
NGC 7582	0.46 ± 0.06	3.31 ± 0.24	0.94 ± 0.03	$1.5\text{-}04$
$\log N_{\text{H},\text{los}}$ - $\log L_X/L_{\text{Edd}}$				
ESO 362-G18 excluded	-0.75 ± 0.16	-1.11 ± 0.46	-0.67 ± 0.07	$6.7\text{-}05$
NGC 1365	-1.23 ± 0.25	-2.11 ± 0.70	-0.85 ± 0.06	$9.3\text{-}04$
NGC 4151	-0.47 ± 0.61	-0.11 ± 1.76	-0.28 ± 0.21	$4.7\text{-}01$
NGC 5548	-0.63 ± 1.86	-1.34 ± 4.44	-0.17 ± 0.27	$7.5\text{-}01$
NGC 7582	-0.07 ± 0.15	1.37 ± 0.59	-0.18 ± 0.22	$6.4\text{-}01$

**Figure 4.** Upper panel: the slope distribution of the correlation between $\log N_{\text{H},\text{los}}$ and $\log L_X/L_{\text{Edd}}$. Lower panel: the probability of the null hypothesis.

4.2 Parameter degeneracy test

To test the variability of $\log N_{\text{H}}$ dependent on $\log L_X/L_{\text{Edd}}$ from the pexrav model is real rather than the degeneracy with parameter Γ , we simulated 200 X-ray spectra (100 for FPMA and 100 for FPMB, respectively) for each observation of the obscured CLAGNs in Table 2 to test parameter degeneracies. The X-ray spectra are simulated with the FAKEIT command using the same reflection model as an input. The input value of the column density from the line of sight is randomly selected from a uniform distribution of values between 10^{22}cm^{-2} and 10^{24}cm^{-2} . The exposure time is set the

same as the original observations. The input value of normalization is selected randomly from the distribution of those values from the previous fitting results. The values for scattering fraction, Γ , high energy cutoff, and reflection factor are randomly selected from distributions following that in Gupta et al. (2021). For the remaining parameters such as redshift, iron abundance, and inclination, we fix them as before in the simulation and fitting.

We present the slope distribution of the correlation between $\log N_{\text{H},\text{los}}$ and $\log L_X/L_{\text{Edd}}$ based on the fitting of the simulated spectra, see Figure 4. We adopt the fitting results with reduced $\chi^2 < 3$. The negative slope for $\log N_{\text{H}}\text{-}\log L_X/L_{\text{Edd}}$ correlation based on spectra fitting significantly deviates from that from simulations. The probability of the Null hypothesis is 1.4×10^{-5} , which further confirms the validity of the reported negative correlation between $\log N_{\text{H},\text{los}}$ and $\log L_X/L_{\text{Edd}}$.

5 DISCUSSION

The changing-state and changing-obscuration phenomena could both be attributed to the change of accretion state or the obscuration effects (e.g., Ricci & Trakhtenbrot 2023). However, the mechanism for the simultaneous variation of X-ray spectra and the column density is under debate. The smooth or clumpy nature of the torus for those changing-look AGNs is still unclear. The rapid variation of X-ray spectra and the column density from the line of sight within a short timescale can also be attributed to the variable obscuration or clumpy nature of absorbing gas for NGC 1365 (Brenneman et al. 2013) and ESO 362-G18 (Ag\'is-Gonz\'alez et al. 2014). One recent work also supports that a fully covering clumpy absorber model could better explain the long-term and short-term absorption variability in NGC 7582 compared to the phenomenological reflection model (see Lefkir et al. 2023). For NGC 5548, the spectral changes could be explained by the emergence of disk wind (Dehghanian et al. 2019; Kriss et al. 2019; Ricci & Trakhtenbrot 2023).

Some other scenarios have also been proposed that the variability of the line-of-sight column density is driven by the change of intrinsic luminosity or the ionization state, which also has a significant impact on the variation of broad emission lines in the BLR as seen in the optical CLAGNs (e.g., Oknyansky et al. 2015; Oknyansky 2022). One possible scenario is that the variation of intrinsic ionizing luminosity could cause the sublimation/condensation of dusty clouds near the central engine (e.g., Jana et al. 2021; Oknyansky 2022). The sublimation timescale ($t_{\text{sub}} \sim 10^{3\text{-}5}\text{s}$) is

much shorter than the typical recovery timescale (\sim several years). The typical optical changing-look AGN NGC 1566 experienced the variation of column density during the 2018 outburst ($N_{\text{H},\text{los}} \sim 3.5 \times 10^{21} \text{ cm}^{-2}$ pre-outburst and recovered from $\sim 6 \times 10^{20} \text{ cm}^{-2}$ to $1.3 \times 10^{21} \text{ cm}^{-2}$ after the outburst; see [Jana et al. 2021](#)). The unobscured nature ($N_{\text{H},\text{los}} < 10^{22} \text{ cm}^{-2}$) of NGC 1566 could be attributed to its face-on view with an inclination angle of $\sim 10^\circ - 18^\circ$ ([Oknyansky et al. 2019](#)). The increase of ionizing luminosity could lead to the dramatic enhancement of broad line emission and the variability of absorption column density through the sublimation of dust ([Oknyansky et al. 2019](#)). In this scenario, [Oknyansky et al. \(2019\)](#) predicts that the $N_{\text{H},\text{los}}$ would recover to the level before the outburst in several years.

Another scenario is that with the increase of the accretion rate and the ionizing luminosity, the increase of the ionization state of the obscuring gas could lead to a decrease in column density. This scenario is originally proposed for NGC 4151 ([Yaqoob et al. 1989](#)). NGC 4151 experienced significant intrinsic changes in the X-ray luminosity and spectral shape (e.g., [Yaqoob et al. 1989; Puccetti et al. 2007; Beuchert et al. 2017](#)). The rapid variability of absorption is consistent with the obscuring material located at BLR (see [Puccetti et al. 2007](#)). Besides, the dust reverberation mapping result for NGC4151 is inconsistent with the prediction of the pure clumpy torus model ([Lyu & Rieke 2021](#)). But a larger amplitude of variations in the luminosity is required for NGC 1365 and other changing-obscuration AGNs than observations in the variable ionization state scenario ([Risaliti et al. 2005; Ricci & Trakhtenbrot 2023](#)).

There is a widely existing positive correlation between the X-ray photon index (Γ) and the Eddington-scaled X-ray 2 – 10 keV luminosity ($\log L_{\text{X}}/L_{\text{Edd}}$, hereafter) to trace the spectral evolution of the corona in bright AGNs (e.g., [Trakhtenbrot et al. 2017](#)). A positive $\Gamma - \log L_{\text{X}}/L_{\text{Edd}}$ correlation (slope ~ 0.19) is also found for the five sources, which is consistent with the positive $\Gamma - \log L_{\text{X}}/L_{\text{Edd}}$ correlation with different slopes varying from 0.1 to 0.3 for individual sources and different samples (e.g., [Trakhtenbrot et al. 2017; Ricci et al. 2018b](#)). The positive $\Gamma - \log L_{\text{X}}/L_{\text{Edd}}$ correlation can be attributed to the seed photons of Compton scattering coming from the thermal emission of SSD (e.g., [Qiao & Liu 2013](#)). In the disc-corona system, the cooling of the electron temperature is more effective and the X-ray spectra become softer with the increase of the accretion rate. The result supports that the five CLAGNs with strong variations of column density are in the SSD (intrinsically type 1) accretion state ([Lyu et al. 2021](#)).

Four of them (i.e., NGC 1365, NGC 4151, NGC 5548, and NGC 7582) produce strong variations of the intrinsic hard X-ray luminosities, which cannot be explained only by the variation of obscuration. The MIR emission is mainly produced by the hot dust heated by the UV radiation from the accretion disc ([Hickox & Alexander 2018](#)), which is less influenced by the obscuration effects. These sources also experienced significant MIR magnitude variabilities based on *WISE* data with $\Delta W1$ of 0.25, 1.13, 0.47, and 0.55 for NGC 1365, NGC 4151, NGC 5548, and NGC 7582, respectively ([Lyu et al. 2022](#)). The MIR magnitude variation of the three AGNs is much larger than normal AGNs ($\Delta W1 \sim 0.1$; [Lyu et al. 2022](#)), which also suggests that the extreme variability of column density can not be simply caused by the obscuration effect.

We find that the line-of-sight column density ($N_{\text{H},\text{los}}$) declined with the increase of the Eddington-scaled X-ray luminosity ($L_{\text{X}}/L_{\text{Edd}}$) for the whole sample except for ESO 362-G18. This suggests that the variation of column density for three CLAGNs is directly regulated by the intrinsic ionizing luminosity (i.e. ac-

cretion rate). The variation of the column density might be driven by the variable winds/outflows forming from the disc at moderate inclination angles (e.g., $\sim 40^\circ - 70^\circ$) from our line of sight (e.g., [Matthews et al. 2020](#)). The disc winds with a certain open angle can push the obscuring material away along the direction of the line of sight and then decrease the column density (e.g., [Mondal et al. 2022](#)). The strength of radiation pressure-driven wind positively correlates with the accretion rate. The negative $\log N_{\text{H},\text{los}} - \log L_{\text{X}}/L_{\text{Edd}}$ correlation supports the disc wind scenario as the explanation of the variability of line-of-sight column density in our sample with moderate inclination angles except for ESO 362-G18. In the scenario of radiation-pressure-driven blowout region (e.g., [Ricci et al. 2017](#)), AGNs with outflows have a higher Eddington ratio between $10^{-1.5}$ and 10^0 . In our sample, NGC 1365, NGC 4151, and NGC 7582 showed significant negative $\log N_{\text{H},\text{los}} - \log L_{\text{X}}/L_{\text{Edd}}$ correlation and had a value of Eddington ratio larger than 10^{-2} . NGC 7582 in the low state had an Eddington ratio smaller than 10^{-2} and it had the lowest variability of column density (see [Figure 3](#)), which is roughly consistent with the radiation-regulated unification of AGN (see Figure 4 in [Ricci et al. 2017](#)). We notice that the slope of $\log N_{\text{H},\text{los}} - \log L_{\text{X}}/L_{\text{Edd}}$ correlation for NGC 1365 is steeper than that of the other sources, which implies the stronger disc wind in NGC 1365.

The hard X-ray observations support the unified scheme for the two kinds of changing-look phenomena (see [Figure 5](#)), which could also naturally explain the observed multi-wavelength (optical/MIR) properties for changing-look AGNs. Similar to changing-state AGNs, changing-obscuration AGNs may be also triggered by the evolution of the accretion disc. Face-on sources with low inclination angles should show little variability of the low column density. For edge-on sources with high inclination angles, the BLRs are fully obscured by the torus. Only sources with moderate inclination angles are expected to show the two kinds of changing-look phenomena, which is consistent with our sample. The disk wind scenario should be only valid in the intrinsically type 1 state (see left part of [Figure 5](#)). When the accretion rate decreases, the ionizing luminosity and the disk wind would be weaker, the obscuration would increase, and the optical state would also transit into the 1.5 or even 1.9 state. In the type 2 state, the plasma is fully ionized by the hot electrons in the ADAF case (e.g., [Liu & Qiao 2022](#)) and the wind may have little influence on the column density (see right part of [Figure 5](#)).

In such a scenario, the variation of the column density should be correlated with the variation of intrinsic luminosity in the smooth torus. For smooth torus, the variations of Γ and $N_{\text{H},\text{los}}$ are both dependent on the change of accretion rate, which is correlated with the strength of the wind. The sources would not experience the abrupt variation of $N_{\text{H},\text{los}}$ while the intrinsic spectra and luminosity do not change a lot. ESO 362-G18 is an outlier in the $\log N_{\text{H},\text{los}} - \log L_{\text{X}}/L_{\text{Edd}}$ correlation, which is consistent with that the variable absorber is attributed to a dusty and clumpy torus ([Agís-González et al. 2014](#)). Thus, the $\log N_{\text{H},\text{los}} - \log L_{\text{X}}/L_{\text{Edd}}$ and $\Gamma - \log L_{\text{X}}/L_{\text{Edd}}$ correlations could be used as a probe for testing the clumpy torus nature for AGNs with extreme variability of column density.

6 CONCLUSIONS

In this work, we explore the X-ray spectral evolution and the variability of column density for five changing-look AGNs based on *NuSTAR* data. All five sources have experienced two types of

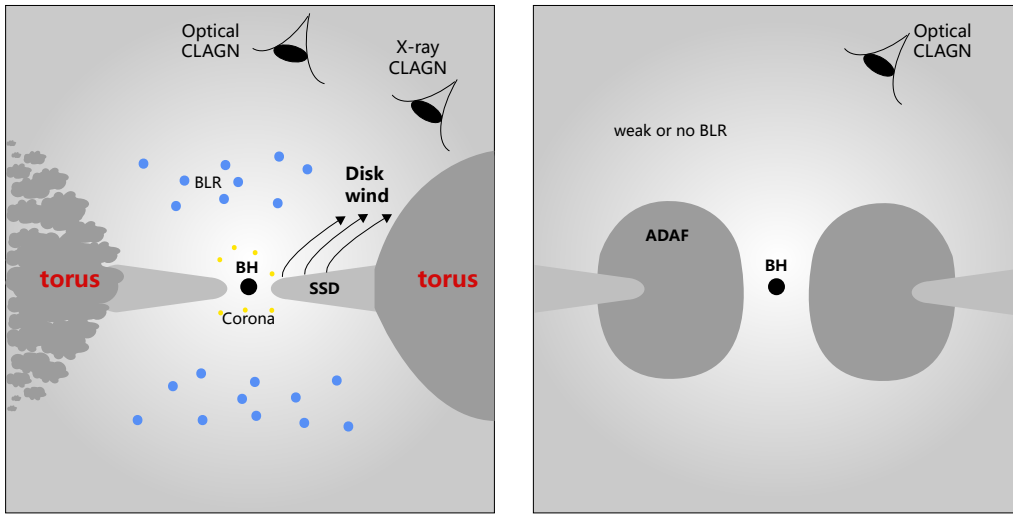


Figure 5. A unified scenario for two kinds of changing-look phenomena. The dusty torus could consist of smooth or clumpy clouds. The optical CLAGNs are face-viewed with low-to-intermediate inclination angles and experience the transition between SSD and ADAF state. The variability of column density in X-ray CLAGNs should be regulated not only by the clumpy torus but also by the disk wind formed at intermediate inclination angles with the change of accretion rate in the SSD state.

changing-look phenomena and have a moderate inclination angle. We summarize the main results as follows:

Based on a phenomenological reflection model pextrav and two clumpy torus models, a significant negative $\log N_{\text{H,los}} - \log L_{\text{X}}/L_{\text{Edd}}$ correlation is found for NGC 1365, NGC 4151, NGC 5548, and NGC 7582. This result supports that the variation of the hydrogen absorption column density is regulated by the variation of intrinsic ionizing luminosity rather than the simple obscuration effect. The variation of the column density might be triggered by the variable wind forming in the disc when observed at an appropriate inclination angle from the line of sight. ESO 362-G18 is an obvious outlier in the $\log N_{\text{H,los}} - \log L_{\text{X}}/L_{\text{Edd}}$ correlation, which could be explained by its clumpy torus structure.

The positive $\Gamma - \log L_{\text{X}}/L_{\text{Edd}}$ correlation supports their SSD accretion mode. For NGC 1365, the slope of the $\Gamma - \log L_{\text{X}}/L_{\text{Edd}}$ correlation is significantly steeper than that of the whole sample. Similarly and interestingly, the slope of the negative $\log N_{\text{H,los}} - \log L_{\text{X}}/L_{\text{Edd}}$ correlation is also significantly steeper for NGC 1365 compared to the whole sample, which implies the stronger disc wind formed in NGC 1365.

The changing-obscuration phenomena are not only modulated by its clumpy torus nature but also mostly possibly triggered by the wind forming in the disc during the evolution of the accretion state with variable accretion rate.

ACKNOWLEDGEMENTS

We are thankful for the support of the National Science Foundation of China (11721303, 11927804, and 12133001) and the National Key R&D Program of China (2022YFF0503401). We acknowledge the science research grant from the China Manned Space Project with No. CMS-CSST-2021-A06. QW was supported in part by the Natural Science Foundation of China (grant U1931203); ZY was supported in part by the Natural Science Foundation of China (grants U1938114), the Youth Innovation Promotion Association of

CAS (id 2020265) and funds for key programs of Shanghai astronomical observatory; and WY would like to acknowledge the support in part by the National Program on Key Research and Development Project (grant 2016YFA0400804) and the National Natural Science Foundation of China (grants 11333005 and U1838203). This research has made use of the NuSTAR Data Analysis Software (NuSTARDAS) package jointly developed by the ASI Space Science Data Center (SSDC, Italy) and the California Institute of Technology (Caltech, USA), and the data provided by the High Energy Astrophysics Science Archive Research Center (HEASARC). This research has made use of NASA's Astrophysics Data System (ADS) and NASA/IPAC EXTRAGALACTIC DATABASE (NED).

DATA AVAILABILITY

The data underlying this article are available through HEASARC Browse database.

REFERENCES

- Agís-González B., et al., 2014, *MNRAS*, **443**, 2862
- Agís-González B., Hutsemékers D., Miniutti G., 2018, *Galaxies*, **6**, 52
- Andonie C., et al., 2022, *A&A*, **664**, A46
- Antonucci R., 1993, *ARA&A*, **31**, 473
- Arnaud K. A., 1996, in Jacoby G. H., Barnes J., eds, Astronomical Society of the Pacific Conference Series Vol. 101, Astronomical Data Analysis Software and Systems V. p. 17
- Baloković M., et al., 2018, *ApJ*, **854**, 42
- Bentz M. C., Katz S., 2015, *PASP*, **127**, 67
- Bentz M. C., Williams P. R., Treu T., 2022, *ApJ*, **934**, 168
- Beuchert T., et al., 2017, *A&A*, **603**, A50
- Bianchi S., Piconcelli E., Chiaberge M., Bailón E. J., Matt G., Fiore F., 2009, *ApJ*, **695**, 781
- Braito V., Reeves J. N., Gofford J., Nardini E., Porquet D., Risaliti G., 2014, *ApJ*, **795**, 87

- Brenneman L. W., Risaliti G., Elvis M., Nardini E., 2013, *MNRAS*, **429**, 2662
- Buchner J., Brightman M., Nandra K., Nikutta R., Bauer F. E., 2019, *A&A*, **629**, A16
- Chen Y.-J., et al., 2023, *MNRAS*, **520**, 1807
- Dehghanian M., et al., 2019, *ApJ*, **882**, L30
- Denney K. D., et al., 2014, *ApJ*, **796**, 134
- Di Gesu L., et al., 2015, *A&A*, **579**, A42
- Elitzur M., Ho L. C., Trump J. R., 2014, *MNRAS*, **438**, 3340
- Fraquelli H. A., Storchi-Bergmann T., Binette L., 2000, *ApJ*, **532**, 867
- Gandhi P., Höning S. F., Kishimoto M., 2015, *ApJ*, **812**, 113
- Grier C. J., et al., 2013, *ApJ*, **773**, 90
- Guo M., Ruschel-Dutra D., Grupe D., Peterson B. M., Storchi-Bergmann T., Schimoia J., Nemmen R., Robinson A., 2021, *MNRAS*, **508**, 144
- Gupta K. K., et al., 2021, *MNRAS*, **504**, 428
- Harrison F. A., et al., 2013, *ApJ*, **770**, 103
- Hickox R. C., Alexander D. M., 2018, *ARA&A*, **56**, 625
- Ho L. C., 2008, *ARA&A*, **46**, 475
- Jana A., Kumari N., Nandi P., Naik S., Chatterjee A., Jaisawal G. K., Hayasaki K., Ricci C., 2021, *MNRAS*, **507**, 687
- Jana A., et al., 2022, *MNRAS*, **512**, 5942
- Jana A., et al., 2024, arXiv e-prints, p. arXiv:2411.08676
- Jin J.-J., Wu X.-B., Feng X.-T., 2022, *ApJ*, **926**, 184
- Kaastra J. S., et al., 2014, *Science*, **345**, 64
- Kalberla P. M. W., Burton W. B., Hartmann D., Arnal E. M., Bajaja E., Morras R., Pöppel W. G. L., 2005, *A&A*, **440**, 775
- Katebi R., et al., 2019, *MNRAS*, **487**, 4057
- Kriss G. A., et al., 2019, *ApJ*, **881**, 153
- LaMassa S. M., et al., 2015, *ApJ*, **800**, 144
- Lefkir M., Kammoun E., Barret D., Boorman P., Matzeu G., Miller J. M., Nardini E., Zoghbi A., 2023, *MNRAS*, **522**, 1169
- Li S.-S., et al., 2022, *ApJ*, **936**, 75
- Liu B. F., Qiao E., 2022, *iScience*, **25**, 103544
- Liu H., Wu Q.-W., Xue Y.-Q., Wang T.-G., Yang J., Guo H.-X., He Z.-C., 2021, *Research in Astronomy and Astrophysics*, **21**, 199
- Liu H., Wu Q., Lyu B., 2022, *ApJ*, **930**, 46
- Lyu J., Rieke G. H., 2021, *ApJ*, **912**, 126
- Lyu B., Yan Z., Yu W., Wu Q., 2021, *MNRAS*, **506**, 4188
- Lyu B., Wu Q., Yan Z., Yu W., Liu H., 2022, *ApJ*, **927**, 227
- MacLeod C. L., et al., 2019, *ApJ*, **874**, 8
- Magdziarz P., Zdziarski A. A., 1995, *MNRAS*, **273**, 837
- Marchesi S., Ajello M., Marcotulli L., Comastri A., Lanzuisi G., Vignali C., 2018, *ApJ*, **854**, 49
- Marchesi S., et al., 2022, *ApJ*, **935**, 114
- Marin F., Porquet D., Goosmann R. W., Dovčiak M., Muleri F., Grossi N., Karas V., 2013, *MNRAS*, **436**, 1615
- Marin F., Hutsemékers D., Agís González B., 2019, in Di Matteo P., Creevey O., Crida A., Kordopatis G., Malzac J., Marquette J. B., N'Diaye M., Venot O., eds, SF2A-2019: Proceedings of the Annual meeting of the French Society of Astronomy and Astrophysics. p. Di (arXiv:1909.02801)
- Matt G., 2002, *Philosophical Transactions of the Royal Society of London Series A*, **360**, 2045
- Matt G., Guainazzi M., Maiolino R., 2003, *MNRAS*, **342**, 422
- Matthews J. H., Knigge C., Higginbottom N., Long K. S., Sim S. A., Mangham S. W., Parkinson E. J., Hewitt H. A., 2020, *MNRAS*, **492**, 5540
- Mehdipour M., Kriss G. A., Kaastra J. S., Costantini E., Gu L., Landt H., Mao J., Rogantini D., 2024, *ApJ*, **962**, 155
- Mondal S., Adhikari T. P., Hryniwicz K., Stalin C. S., Pandey A., 2022, *A&A*, **662**, A77
- Netzer H., 2015, *ARA&A*, **53**, 365
- Netzer H., 2019, *MNRAS*, **488**, 5185
- Neustadt J. M. M., et al., 2023, *MNRAS*,
- Noda H., Done C., 2018, *MNRAS*, **480**, 3898
- Noda H., et al., 2022, arXiv e-prints, p. arXiv:2212.02731
- Oh K., et al., 2022, *ApJS*, **261**, 4
- Oknyanskij V. L., Metlova N. V., Huseynov N. A., Guo D.-F., Lyuty V. M., 2016, *Odessa Astronomical Publications*, **29**, 95
- Oknyanskij V., 2022, *Astronomische Nachrichten*, **343**, e210080
- Oknyanskij V. L., Gaskell C. M., Shimanovskaya E. V., 2015, *Odessa Astronomical Publications*, **28**, 175
- Oknyanskij V. L., Winkler H., Tsygankov S. S., Lipunov V. M., Gorbovskoy E. S., van Wyk F., Buckley D. A. H., Tyurina N. V., 2019, *MNRAS*, **483**, 558
- Onori F., et al., 2017, *MNRAS*, **468**, L97
- Osterbrock D. E., 1981, *ApJ*, **249**, 462
- Osterbrock D. E., Koski A. T., 1976, *MNRAS*, **176**, 61P
- Pal I., Stalin C. S., Mallick L., Rani P., 2022, *A&A*, **662**, A78
- Pancoast A., Brewer B. J., Treu T., Park D., Barth A. J., Bentz M. C., Woo J.-H., 2014, *MNRAS*, **445**, 3073
- Panda S., Śniegowska M., 2024, *ApJS*, **272**, 13
- Paturel G., Petit C., Prugniel P., Theureau G., Rousseau J., Brouty M., Dubois P., Cambresy L., 2003, *A&A*, **412**, 45
- Piconcelli E., Bianchi S., Guainazzi M., Fiore F., Chiaberge M., 2007, *A&A*, **466**, 855
- Potts B., Villforth C., 2021, *A&A*, **650**, A33
- Puccetti S., Fiore F., Risaliti G., Capalbi M., Elvis M., Nicastro F., 2007, *MNRAS*, **377**, 607
- Qiao E., Liu B. F., 2013, *ApJ*, **764**, 2
- Raimundo S. I., Vestergaard M., Koay J. Y., Lawther D., Casasola V., Peterson B. M., 2019, *MNRAS*, **486**, 123
- Ricci C., Trakhtenbrot B., 2023, *Nature Astronomy*, **7**, 1282
- Ricci C., et al., 2016, *ApJ*, **820**, 5
- Ricci C., et al., 2017, *Nature*, **549**, 488
- Ricci T. V., Steiner J. E., May D., Garcia-Rissmann A., Menezes R. B., 2018a, *MNRAS*, **473**, 5334
- Ricci C., et al., 2018b, *MNRAS*, **480**, 1819
- Risaliti G., Elvis M., Fabbiano G., Baldi A., Zezas A., 2005, *ApJ*, **623**, L93
- Risaliti G., et al., 2009, *MNRAS*, **393**, L1
- Rivers E., et al., 2015, *ApJ*, **815**, 55
- Senarath M. R., et al., 2021, *MNRAS*, **503**, 2583
- Shakura N. I., Sunyaev R. A., 1973, *A&A*, **24**, 337
- Shappee B. J., et al., 2014, *ApJ*, **788**, 48
- Sheng Z., Wang T., Jiang N., Yang C., Yan L., Dou L., Peng B., 2017, *ApJ*, **846**, L7
- Sheng Z., et al., 2020, *ApJ*, **889**, 46
- Śniegowska M., Czerny B., Bon E., Bon N., 2020, *A&A*, **641**, A167
- Tanimoto A., Ueda Y., Odaka H., Kawaguchi T., Fukazawa Y., Kawamuro T., 2019, *ApJ*, **877**, 95
- Tanimoto A., Ueda Y., Odaka H., Yamada S., Ricci C., 2022, *ApJS*, **260**, 30
- Temple M. J., et al., 2023, *MNRAS*, **518**, 2938
- Trakhtenbrot B., et al., 2017, *MNRAS*, **470**, 800
- Trakhtenbrot B., et al., 2019, *ApJ*, **883**, 94
- Turner T. J., Reeves J. N., Braito V., Lobban A., Kraemer S., Miller L., 2018, *MNRAS*, **481**, 2470
- Walton D. J., Reis R. C., Fabian A. C., 2010, *MNRAS*, **408**, 601
- Wang J., Xu D. W., Wang Y., Zhang J. B., Zheng J., Wei J. Y., 2019, *ApJ*, **887**, 15
- Wang J., Xu D. W., Wei J. Y., 2020, *ApJ*, **901**, 1
- Wang J., Zheng W. K., Xu D. W., Brink T. G., Filippenko A. V., Gao C., Sun S. S., Wei J. Y., 2022, *Research in Astronomy and Astrophysics*, **22**, 015011
- Wold M., Lacy M., Käufel H. U., Siebenmorgen R., 2006, *A&A*, **460**, 449
- Yang Q., et al., 2018, *ApJ*, **862**, 109
- Yang Q., et al., 2023, *ApJ*, **953**, 61
- Yaqoob T., Warwick R. S., Pounds K. A., 1989, *MNRAS*, **236**, 153
- Yuan F., Narayan R., 2014, *ARA&A*, **52**, 529
- Zeltyn G., et al., 2022, *ApJ*, **939**, L16
- Zeltyn G., et al., 2024, *ApJ*, **966**, 85
- Zhong X.-G., Wang J.-C., 2022, *Research in Astronomy and Astrophysics*, **22**, 035002

APPENDIX A: SAMPLE

A1 ESO 362-G18

ESO 362-G18 is a nearby ($z = 0.0124$) Seyfert galaxy with BH mass $\log(M_{\text{BH}}/M_{\odot}) = 7.65$ and a high black hole spin $a \geq 0.92$ (see Agís-González et al. 2014, 2018, and references therein). An inclination ($i = 53^\circ \pm 5^\circ$) between the disc axis and our line-of-sight is well constrained through a disc-reflection component accounting for the broad Fe K α line and hard X-ray band above 10 keV (Fraquelli et al. 2000; Agís-González et al. 2014).

ESO 362-G18 was classified as Seyfert (Sy) 1.5, however, experienced multiple times of variations of broad emission lines. Based on four spectra of different epochs, Agís-González et al. (2018) reported the Sy1.9 classification in 6dF (30 Jan 2003) and EFOSC1 (21 Sep 2006) data and Sy1.5 classification with evident broad emission lines (especially for H β lines) in EMMI (18 Sep 2004) and FORS2 (29 Mar 2016) data.

ESO 362-G18 also showed highly variable column density with a mild absorption ($N_{\text{H}} \sim 0.5 \times 10^{22} \text{ cm}^{-2}$) in *Swift* data (26 Nov 2005). A more heavy absorption ($N_{\text{H}} \sim 3 - 4 \times 10^{23} \text{ cm}^{-2}$) by two orders of magnitude was found after 2 months (28 Jan 2006) in *XMM-Newton* data. The absorption returned to $N_{\text{H}} \lesssim 3 \times 10^{22} \text{ cm}^{-2}$ in *Suzaku*, *XMM-Newton*, and *Chandra* data during 2008–2010 (Agís-González et al. 2014).

A2 NGC 1365

NGC 1365 is nearby ($z = 0.0055$) Seyfert galaxy with a BH mass $\log(M_{\text{BH}}/M_{\odot}) = 6.65$ (Onori et al. 2017). Based on the *Suzaku* data, the inclination angle of the accretion disc ($i = 57^\circ_{-2^\circ}$) was constrained with a disc reflection component (Walton et al. 2010). NGC 1365 was a well-known Changing-obscuration AGN with a rapid X-ray spectral state change from Compton-thick to Compton-thin and back again in 2002 and 2003. Significant variability of hydrogen column density and strong spectral evolution in optical and X-ray were also found between 2012 and 2013 based on *XMM-Newton* and *NuSTAR* data (Liu et al. 2021). NGC 1365 also experienced multiple times of rapid variations of broad Balmer lines during the past years. NGC 1365 was originally observed to show broad Balmer lines in 1993 August and then turned into a faint state with only narrow H β and weak broad H α lines in 2009 January and 2010 September. It turned back on with broad Balmer lines in 2013 January, 2013 December, 2014 October, and 2017 June spectra and returned to the turning-off state with only narrow lines newly discovered in 2021 December (see Temple et al. 2023, and references therein).

A3 NGC 4151

NGC 4151 is a well-studied nearby ($z = 0.0033$) changing-look Seyfert galaxy with BH mass $\log(M_{\text{BH}}/M_{\odot})$ around 7.56 (e.g. Grier et al. 2013). A thick disc with an inclination ($i \sim 58.1^\circ_{-9.6^\circ}$) was estimated (Bentz et al. 2022), which is consistent with constraints from geometric modeling of the narrow-line region in previous works and the BLR gas cloud temporarily obscured the central X-ray emission (see details in Bentz et al. 2022).

NGC 4151 experienced a rapid change of $N_{\text{H}} \sim 10^{22} - 10^{23} \text{ cm}^{-2}$ in 1996 July and 2001 Dec (see Puccetti et al. 2007). NGC 4151 also experienced strong historic variability (e.g., Oknyanskij et al. 2016) and multiple optical spectral type changes from Sy1 in 1974 to Sy1.9 during 1984–1989 and to Sy1.5 during

1990–1998 and to Sy1.8 in 2001 (e.g., Marin et al. 2019). The broad H β lines are visible between 2005 February 27 and 2005 April 10 in a reverberation mapping program (Bentz et al. 2022). The long-term reverberation mapping campaigns of NGC 4151 also show the broad H β lines since 2018 (e.g., Li et al. 2022; Chen et al. 2023).

A4 NGC 5548

NGC 5548 is a well-known Seyfert 1 galaxy with BH mass $\log(M_{\text{BH}}/M_{\odot})$ around 7.7 (e.g. Bentz & Katz 2015). A narrow thick disk with an inclination angle ($i = 38.8^\circ_{-11.4^\circ}$) is constrained for the geometry of H β BLR (Pancoast et al. 2014). NGC 5548 showed a clear changing-obscuration event in 2013 with two obscuring components, which lasted several years (Kaastra et al. 2014; Ricci & Trakhtenbrot 2023). NGC 5548 also showed variations of both the intrinsic continuum and the obscurer (Di Gesu et al. 2015; Kriss et al. 2019; Sniegowska et al. 2020; Mehdiour et al. 2024). NGC 5548 experienced transitions from type 1.0 (1978–2001) to type 1.8 (2005–2007) and to 1.0 (2014–2021; see Jana et al. 2024).

A5 NGC 7582

NGC 7582 is a nearby ($z = 0.0053$) changing-look Seyfert galaxy with BH mass $\log(M_{\text{BH}}/M_{\odot}) = 7.74$ (Ricci et al. 2018a) and an galactic inclination angle of ($i = 68^\circ$) (e.g. Paturel et al. 2003), which exhibits complex and variable X-ray spectra. A lower limit for the disk inclination angle $i \sim 70.8^\circ_{-10.6^\circ}$ was constrained for NGC 7582 through X-ray spectral fitting based on the *NuSTAR* data combined with the simultaneous *XMM-Newton* data (see Tanimoto et al. 2022). An inclination angle ($i = 80^\circ$) of the line of sight to the disk was used to fit the X-ray spectra of NGC 7582 as a Seyfert 2 (Lefkir et al. 2023).

Piconcelli et al. (2007) found that both the X-ray spectral index (Γ) and $N_{\text{H},\text{los}}$ are variable with *XMM-Newton* data. Rapid variations of column density from an inner absorber ($N_{\text{H},i}$ ranged between $3.3 - 12 \times 10^{23} \text{ cm}^{-2}$ down to timescales of less than a day) was monitored by *Suzaku* and *XMM-Newton* during 2007 (Bianchi et al. 2009). NGC 7582 became more heavily absorbed $N_{\text{H},\text{los}} \sim (3.1 \pm 0.7) \times 10^{23} \text{ cm}^{-2}$ in 2012 (see Rivers et al. 2015; Marchesi et al. 2018) and $N_{\text{H},\text{los}} \sim (3.6 \pm 0.4) \times 10^{23} \text{ cm}^{-2}$ in 2016 (Baloković et al. 2018) based on the *NuSTAR* data. Besides, NGC 7582 was type 1 in 1977 and experienced a fast optical type change from type 1 to type 1.8 in 1998, then to type 2 between 2004 and 2016 (see Oh et al. 2022; Jana et al. 2024).

APPENDIX B: FITTING RESULTS

This paper has been typeset from a *T_EX/L_AT_EX* file prepared by the author.

Table B1. The parameters of five CLAGNs fitted with `pexrav` model. The table lists the Name, ObsID, cross constant of instruments (FPMB and soft X-ray observations) relative to FPMA, line-of-sight column density in the unit of 10^{22} cm^{-2} , photon index, cutoff energy, normalization in units of photons/ $\text{keV}/\text{cm}^2/\text{s}$, line energy, sigma, and normalization the Fe $\text{K}\alpha$, reflection factor (R), scatter fraction (fscat), χ^2/dof , and the observed flux, and intrinsic flux at 2-10 keV band in units of $\text{erg}/\text{s}/\text{cm}^{-2}$. f means the value is fixed during the fitting.

Name	ObsID	Cross constant zgaussnorm	$N_{\text{H},\text{los}}$ R	Γ fscat	Ecut [keV] $\chi^2_r(\chi^2/\text{dof})$	Norm $\log f_{\text{obs},2-10\text{keV}}$	zgauss $\log f_{\text{int},2-10\text{keV}}$	sigma
ESO362-G18	60201046002/790810101	0.980 \pm 0.008/0.669 \pm 0.005	0.00 f	1.49 \pm 0.00	200 f	2.11e-03 \pm 2.14e-05	6.38 \pm 0.01	0.05 \pm 0.01
		2.91e-05 \pm 1.21e-06	0.00 \pm 0.00	0.00 \pm 0.00	1.14(3104/2729)	-10.931 \pm 0.001	-10.942 \pm 0.001	
NGC1365	60002046002/692840201	1.018 \pm 0.013/0.901 \pm 0.010	21.15 \pm 0.71	1.80 \pm 0.03	200 f	6.42e-03 \pm 4.01e-04	6.35 \pm 0.01	0.05 f
		2.10e-05 \pm 1.16e-06	-1.10 \pm 0.16	0.00 \pm 0.01	1.30(2684/2064)	-11.017 \pm 0.003	-10.790 \pm 0.004	
NGC1365	60002046003/35458003	1.015 \pm 0.012/0.633 \pm 0.058	15.08 \pm 1.31	1.65 \pm 0.09	289 \pm 211	4.30e-03 \pm 8.08e-04	6.20 \pm 0.09	0.19 \pm 0.07
		2.70e-05 \pm 5.95e-06	-1.00 \pm 0.42	0.05 \pm 0.01	1.16(905/779)	-10.964 \pm 0.002	-10.726 \pm 0.006	
NGC1365	60702058002/96123002	1.032 \pm 0.013/0.490 \pm 0.049	21.28 \pm 2.53	1.65 \pm 0.05	200 f	2.49e-03 \pm 2.03e-04	6.28 \pm 0.03	0.05 f
		1.89e-05 \pm 2.07e-06	-2.46 \pm 0.41	0.05 \pm 0.03	1.08(815/754)	-11.171 \pm 0.003	-10.979 \pm 0.005	
NGC1365	60702058004/89213003	1.034 \pm 0.015/1.247 \pm 0.111	25.81 \pm 3.07	1.79 \pm 0.05	200 f	3.49e-03 \pm 3.30e-04	6.21 \pm 0.06	0.05 f
		1.74e-05 \pm 2.60e-06	-3.21 \pm 0.66	0.04 \pm 0.03	1.03(590/572)	-11.155 \pm 0.003	-10.924 \pm 0.005	
NGC1365	60702058006	1.025 \pm 0.031	36.61 \pm 10.50	1.76 \pm 0.10	200 f	2.07e-03 \pm 6.00e-04	6.34 \pm 0.07	0.05 f
		1.33e-05 \pm 4.14e-06	-5.69 \pm 3.07	0.00 \pm 0.06	1.01(164/163)	-11.331 \pm 0.007	-11.126 \pm 0.006	
NGC1365	60702058008	1.037 \pm 0.014	13.95 \pm 0.81	1.70 \pm 0.05	200 f	3.11e-03 \pm 2.69e-04	6.40 \pm 0.03	0.05 f
		2.03e-05 \pm 2.49e-06	-2.10 \pm 0.38	0.00 \pm 3.86	1.16(778/670)	-11.099 \pm 0.003	-10.906 \pm 0.039	
NGC1365	60702058010	1.055 \pm 0.015	28.84 \pm 5.16	1.53 \pm 0.14	94 \pm 35	1.73e-03 \pm 4.90e-04	6.28 \pm 0.03	0.05 f
		1.59e-05 \pm 2.48e-06	-3.34 \pm 0.73	0.05 \pm 0.03	1.07(627/586)	-11.252 \pm 0.003	-11.063 \pm 0.070	
NGC1365	60702058012	1.004 \pm 0.017	87.16 \pm 14.27	1.53 \pm 0.16	149 \pm 97	1.85e-03 \pm 9.62e-04	6.33 \pm 0.02	0.05 f
		1.52e-05 \pm 1.75e-06	-2.37 \pm 0.86	0.05 \pm 0.03	1.08(557/515)	-11.506 \pm 0.004	-11.026 \pm 0.009	
NGC4151	60001111002/80073001	0.980 \pm 0.004/0.577 \pm 0.022	5.23 \pm 0.24	1.51 \pm 0.02	64 \pm 3	4.89e-02 \pm 2.26e-03	6.26 \pm 0.02	0.20 \pm 0.03
		3.13e-04 \pm 2.83e-05	-0.67 \pm 0.06	0.03 \pm 0.01	1.11(1715/1550)	-9.676 \pm 0.001	-9.677 \pm 0.007	
NGC4151	60001111003/80073001	0.997 \pm 0.002/0.768 \pm 0.028	7.07 \pm 0.20	1.39 \pm 0.02	62 \pm 2	3.73e-02 \pm 1.29e-03	6.26 \pm 0.01	0.22 \pm 0.01
		4.10e-04 \pm 1.80e-05	-0.47 \pm 0.03	0.04 \pm 0.01	1.12(2287/2035)	-9.743 \pm 0.001	-9.611 \pm 0.003	
NGC4151	60001111005	0.999 \pm 0.002	17.67 \pm 0.75	1.70 \pm 0.02	126 \pm 10	6.45e-02 \pm 2.97e-03	6.31 \pm 0.01	0.05 f
		2.26e-04 \pm 1.10e-05	-0.78 \pm 0.04	0.39 \pm 0.01	1.16(2333/2020)	-9.663 \pm 0.000	-9.601 \pm 0.003	
NGC4151	60502017002	0.988 \pm 0.003	17.86 \pm 0.99	1.70 \pm 0.03	141 \pm 18	6.37e-02 \pm 4.11e-03	6.27 \pm 0.01	0.05 f
		2.38e-04 \pm 1.43e-05	-0.52 \pm 0.05	0.27 \pm 0.01	1.07(1723/1613)	-9.752 \pm 0.001	-9.603 \pm 0.004	
NGC4151	60502017004/88889001	0.999 \pm 0.002	14.30 \pm 0.92	1.76 \pm 0.02	187 \pm 24	7.40e-02 \pm 3.49e-03	6.29 \pm 0.01	0.05 f
		2.39e-04 \pm 1.39e-05	-0.72 \pm 0.04	0.44 \pm 0.02	1.02(1890/1847)	-9.595 \pm 0.001	-9.574 \pm 0.004	
NGC4151	60502017006	0.992 \pm 0.003	13.61 \pm 1.25	1.75 \pm 0.02	150 \pm 19	6.24e-02 \pm 3.71e-03	6.29 \pm 0.01	0.05 f
		2.53e-04 \pm 1.60e-05	-0.81 \pm 0.06	0.58 \pm 0.03	1.03(1684/1637)	-9.599 \pm 0.001	-9.648 \pm 0.006	
NGC4151	60502017008/88889004	0.984 \pm 0.003	18.91 \pm 1.14	1.71 \pm 0.03	130 \pm 17	5.73e-02 \pm 4.23e-03	6.29 \pm 0.01	0.05 f
		2.33e-04 \pm 1.46e-05	-0.77 \pm 0.06	0.34 \pm 0.02	1.11(1727/1551)	-9.755 \pm 0.001	-9.657 \pm 0.005	
NGC4151	60502017010	0.976 \pm 0.003	19.67 \pm 1.16	1.73 \pm 0.03	168 \pm 28	6.13e-02 \pm 4.70e-03	6.29 \pm 0.01	0.05 f
		2.23e-04 \pm 1.52e-05	-0.62 \pm 0.06	0.39 \pm 0.02	1.09(1688/1549)	-9.725 \pm 0.001	-9.638 \pm 0.005	
NGC4151	60502017012/88889005	0.978 \pm 0.004	17.81 \pm 1.31	1.70 \pm 0.03	201 \pm 41	5.25e-02 \pm 4.21e-03	6.31 \pm 0.01	0.05 f
		2.81e-04 \pm 1.59e-05	-0.59 \pm 0.06	0.47 \pm 0.02	1.04(1592/1527)	-9.717 \pm 0.001	-9.686 \pm 0.006	
NGC5548	60002044002/91744028	1.002 \pm 0.008/0.750 \pm 0.042	1.37 \pm 0.44	1.57 \pm 0.03	196 \pm 79	9.33e-03 \pm 7.19e-04	6.20 \pm 0.19	0.45 \pm 0.11
		7.41e-05 \pm 1.67e-05	-0.10 \pm 0.07	0.05 \pm 0.11	1.01(896/890)	-10.361 \pm 0.002	-10.340 \pm 0.043	
NGC5548	60002044003/91711077	1.015 \pm 0.008/0.795 \pm 0.051	1.76 \pm 0.35	1.69 \pm 0.03	165 \pm 50	1.10e-02 \pm 6.01e-04	6.35 \pm 1.28	0.00 \pm 0.03
		3.20e-05 \pm 5.88e-06	-0.38 \pm 0.09	0.05 \pm 0.05	1.04(902/864)	-10.383 \pm 0.002	-10.361 \pm 0.036	
NGC5548	60002044005/91744040	0.985 \pm 0.006/0.094 \pm 0.049	2.86 \pm 1.10	1.55 \pm 0.04	113 \pm 21	7.77e-03 \pm 2.02e-03	6.32 \pm 0.02	0.06 \pm 0.06
		4.68e-05 \pm 5.56e-06	-0.25 \pm 0.09	0.05 \pm 0.29	0.96(1044/1086)	-10.471 \pm 0.001	-10.433 \pm 0.025	
NGC5548	60002044006/91711139	1.017 \pm 0.006/0.094 \pm 0.044	0.89 \pm 1.21	1.64 \pm 0.04	119 \pm 23	9.74e-03 \pm 1.06e-02	6.35 \pm 0.03	0.19 \pm 0.04
		5.57e-05 \pm 7.39e-06	-0.35 \pm 0.40	0.05 \pm 1.17	1.03(1121/1092)	-10.375 \pm 0.001	-10.404 \pm 0.055	
NGC5548	60002044008/80131001	0.977 \pm 0.007/0.692 \pm 0.044	1.88 \pm 0.42	1.40 \pm 0.03	64 \pm 6	5.15e-03 \pm 3.26e-04	6.35 \pm 0.02	0.14 \pm 0.04
		5.56e-05 \pm 5.64e-06	-0.29 \pm 0.07	0.05 \pm 0.07	1.04(1132/1084)	-10.512 \pm 0.001	-10.488 \pm 0.029	
NGC5548	90701601002/95671036	1.007 \pm 0.008/0.819 \pm 0.059	0.85 \pm 0.48	1.63 \pm 0.03	175 \pm 54	7.95e-03 \pm 1.79e-03	6.34 \pm 0.03	0.14 \pm 0.04
		5.35e-05 \pm 6.48e-06	-0.33 \pm 0.13	0.05 \pm 0.28	0.98(940/959)	-10.447 \pm 0.002	-10.433 \pm 0.038	
NGC7582	60061318002/32534001	0.968 \pm 0.021/0.960 \pm 0.106	24.89 \pm 2.18	1.32 \pm 0.09	200 f	1.68e-03 \pm 3.04e-04	6.36 \pm 0.03	0.05 f
		2.64e-05 \pm 3.94e-06	-1.00 \pm 0.78	0.05 \pm 0.01	1.12(336/301)	-11.177 \pm 0.005	-11.110 \pm 0.039	
NGC7582	60061318004	0.987 \pm 0.026	51.18 \pm 13.15	1.42 \pm 0.08	104 f	1.08e-03 \pm 3.83e-04	6.37 \pm 0.03	0.05 f
		2.32e-05 \pm 3.34e-06	-4.96 \pm 2.76	0.10 \pm 0.03	1.09(231/212)	-11.349 \pm 0.006	-11.192 \pm 0.070	
NGC7582	60201003002/782720301	0.992 \pm 0.009/0.676 \pm 0.008	34.51 \pm 0.79	1.62 \pm 0.03	200 f	9.63e-03 \pm 7.30e-04	6.39 \pm 0.01	0.05 f
		2.95e-05 \pm 1.98e-06	-0.29 \pm 0.09	0.02 \pm 0.00	1.41(3880/2754)	-10.912 \pm 0.002	-10.546 \pm 0.009	

Table B2. The parameters fitted with the xclumpy model. The table lists the Name, ObsID, cross constant of instruments (FPMB and soft X-ray observations relative to FPMA, line-of-sight column density, photon index, scatter fraction (fscat), inclination angle, χ^2/dof , and the intrinsic 2–10 keV flux and luminosity.

Name	ObsID	Cross constant sigma degree	$N_{\text{H,los}} [10^{22} \text{ cm}^{-2}]$ AL	$N_{\text{H,tor}} [10^{24} \text{ cm}^{-2}]$ fscat	Γ χ^2/dof	Norm [photons/keV/cm ² /s] $\log f_{\text{int},2-10\text{keV}}$	Inclination angle $\log L_{\text{int},2-10\text{keV}}$
ESO362-G18	60201046002	0.981±0.008 18.5 ± 4.6	1.2±0.4 1.7 ± 0.6	3.8 ± 1.3 0.00±1.00	1.68 ± 0.04 0.87(417/479)	2.91e-03 ± 2.22e-04 -10.921 ± 0.017	45 ± 10 42.616 ± 0.017
NGC1365	60002046002	1.020±0.015 19.8 ± 1.7	19.2±7.1 0.9 ± 0.3	10.0 ± 3.7 0.09±0.03	1.66 ± 0.04 1.10(380/346)	4.39e-03 ± 5.09e-04 -10.724 ± 0.076	50 ± 2 42.102 ± 0.076
NGC1365	60002046003	1.010±0.012 19.2 ± 1.7	15.2±5.6 0.9 ± 0.3	10.0 ± 3.7 0.04±0.05	1.64 ± 0.04 1.15(448/391)	4.77e-03 ± 4.15e-04 -10.674 ± 0.048	50 ± 2 42.152 ± 0.048
NGC1365	60702058002	1.030±0.015 20.9 ± 1.9	28.6±10.6 2.0 ± 0.3	10.0 ± 3.7 0.14±0.02	1.49 ± 0.04 1.18(458/387)	2.48e-03 ± 3.34e-04 -10.854 ± 0.123	50 ± 2 41.972 ± 0.123
NGC1365	60702058004	1.040±0.018 21.4 ± 2.0	34.3±12.7 1.1 ± 0.3	10.0 ± 3.7 0.10±0.01	1.62 ± 0.06 1.14(333/293)	4.05e-03 ± 7.46e-04 -10.731 ± 0.138	50 ± 2 42.095 ± 0.138
NGC1365	60702058006	1.020±0.036 23.2 ± 2.2	55.9±20.7 1.2 ± 0.4	10.0 ± 3.7 0.07±0.02	1.60 ± 0.09 1.03(87/85)	4.31e-03 ± 1.38e-03 -10.690 ± 0.330	50 ± 2 42.136 ± 0.330
NGC1365	60702058008	1.040±0.014 18.9 ± 1.7	12.9±4.8 1.7 ± 0.5	10.0 ± 3.7 0.00±0.03	1.48 ± 0.03 1.20(416/347)	2.46e-03 ± 1.94e-04 -10.850 ± 0.060	50 ± 2 41.976 ± 0.060
NGC1365	60702058010	1.060±0.018 22.8 ± 2.1	51.0±18.9 1.1 ± 0.2	10.0 ± 3.7 0.08±0.01	1.63 ± 0.06 1.14(344/302)	4.66e-03 ± 8.99e-04 -10.677 ± 0.153	50 ± 2 42.149 ± 0.153
NGC1365	60702058012	0.998±0.020 25.5 ± 2.6	91.5±33.9 1.3 ± 0.2	10.0 ± 3.7 0.06±0.01	1.63 ± 0.06 1.01(270/269)	4.91e-03 ± 1.07e-03 -10.654 ± 0.159	50 ± 2 42.172 ± 0.159
NGC4151	60001111002	0.960±0.006 24.2 ± 1.2	23.7±1.9 0.5 ± 0.1	4.5 ± 0.4 0.44±0.02	1.84 ± 0.01 1.08(806/748)	8.26e-02 ± 4.49e-03 -9.569 ± 0.042	48 ± 1 42.812 ± 0.042
NGC4151	60001111003	0.995±0.003 23.8 ± 1.2	21.4±1.7 0.8 ± 0.0	4.5 ± 0.4 0.28±0.01	1.78 ± 0.01 1.03(1015/987)	7.59e-02 ± 2.24e-03 -9.566 ± 0.022	48 ± 1 42.815 ± 0.022
NGC4151	60001111005	0.998±0.003 23.3 ± 1.2	19.1±1.5 0.7 ± 0.0	4.5 ± 0.4 0.35±0.01	1.80 ± 0.01 1.15(1168/1018)	8.19e-02 ± 2.29e-03 -9.546 ± 0.020	48 ± 1 42.835 ± 0.020
NGC4151	60502017002	0.981±0.004 23.2 ± 1.2	18.6±1.5 0.7 ± 0.1	4.5 ± 0.4 0.23±0.01	1.83 ± 0.01 1.09(892/819)	8.54e-02 ± 3.01e-03 -9.548 ± 0.028	48 ± 1 42.833 ± 0.028
NGC4151	60502017004	0.997±0.004 22.1 ± 1.1	13.2±1.1 0.8 ± 0.1	4.5 ± 0.4 0.38±0.02	1.79 ± 0.01 1.03(964/938)	8.15e-02 ± 1.90e-03 -9.541 ± 0.018	48 ± 1 42.839 ± 0.018
NGC4151	60502017006	0.985±0.005 22.3 ± 1.1	14.1±1.1 0.9 ± 0.1	4.5 ± 0.4 0.51±0.03	1.81 ± 0.01 1.09(911/833)	7.41e-02 ± 2.45e-03 -9.596 ± 0.027	48 ± 1 42.785 ± 0.027
NGC4151	60502017008	0.978±0.005 23.4 ± 1.2	19.8±1.6 0.8 ± 0.1	4.5 ± 0.4 0.31±0.01	1.80 ± 0.01 1.07(843/785)	7.12e-02 ± 2.79e-03 -9.607 ± 0.033	48 ± 1 42.774 ± 0.033
NGC4151	60502017010	0.961±0.005 23.4 ± 1.2	19.5±1.6 0.8 ± 0.1	4.5 ± 0.4 0.34±0.01	1.81 ± 0.01 1.12(883/788)	7.39e-02 ± 3.08e-03 -9.597 ± 0.034	48 ± 1 42.783 ± 0.034
NGC4151	60502017012	0.964±0.006 22.8 ± 1.1	16.7±1.3 1.2 ± 0.1	4.5 ± 0.4 0.41±0.02	1.76 ± 0.01 1.02(798/780)	5.97e-02 ± 2.34e-03 -9.656 ± 0.034	48 ± 1 42.724 ± 0.034
NGC5548	60002044002	1.000±0.024 33.9 ± 5.2	18.1±2.7 0.7 ± 0.3	4.0 ± 0.6 1.39±0.21	1.80 ± 0.04 0.98(417/428)	7.38e-03 ± 1.40e-03 -10.602 ± 0.187	30 ± 8 43.221 ± 0.187
NGC5548	60002044003	1.020±0.012 27.5 ± 4.6	3.7±0.6 0.5 ± 0.2	4.0 ± 0.6 0.33±0.34	1.81 ± 0.04 0.99(409/416)	1.09e-02 ± 3.33e-03 -10.439 ± 0.137	30 ± 8 43.384 ± 0.137
NGC5548	60002044005	0.958±0.014 33.3 ± 5.1	16.3±2.5 1.1 ± 0.2	4.0 ± 0.6 0.94±0.09	1.78 ± 0.03 0.94(505/540)	7.14e-03 ± 7.88e-04 -10.603 ± 0.132	30 ± 8 43.220 ± 0.132
NGC5548	60002044006	1.020±0.008 26.1 ± 4.2	2.1±0.3 0.8 ± 0.2	4.0 ± 0.6 0.16±0.22	1.81 ± 0.03 1.05(564/539)	1.20e-02 ± 2.75e-03 -10.398 ± 0.097	30 ± 8 43.425 ± 0.097
NGC5548	60002044008	0.948±0.014 34.7 ± 5.3	21.2±3.2 0.9 ± 0.2	4.0 ± 0.6 0.79±0.07	1.80 ± 0.03 0.91(488/535)	7.97e-03 ± 9.91e-04 -10.568 ± 0.132	30 ± 8 43.254 ± 0.132
NGC5548	90701601002	1.010±0.009 26.3 ± 4.3	2.3±0.4 1.0 ± 0.2	4.0 ± 0.6 0.20±0.28	1.78 ± 0.03 0.93(440/474)	9.34e-03 ± 2.65e-03 -10.486 ± 0.122	30 ± 8 43.337 ± 0.122
NGC7582	60061318002	0.956±0.027 16.9 ± 4.0	43.1±33.1 3.6 ± 1.6	9.9 ± 7.7 0.14±0.05	1.39 ± 0.07 1.12(169/151)	2.47e-03 ± 8.78e-04 -10.785 ± 0.150	60 ± 10 42.009 ± 0.150
NGC7582	60061318004	0.985±0.032 18.6 ± 4.7	73.0±56.1 2.7 ± 1.1	9.9 ± 7.7 0.08±0.03	1.44 ± 0.10 1.14(128/113)	3.28e-03 ± 1.60e-03 -10.697 ± 0.176	60 ± 10 42.096 ± 0.176
NGC7582	60201003002	0.991±0.010 16.2 ± 3.8	32.0±24.6 1.2 ± 0.5	9.9 ± 7.7 0.06±0.03	1.64 ± 0.05 1.06(519/491)	8.24e-03 ± 2.17e-03 -10.436 ± 0.051	60 ± 10 42.357 ± 0.051

Table B3. The parameters fitted with the uxclumpy model. The table lists the Name, ObsID, cross constant of instruments (FPMB and soft X-ray observations relative to FPMA, line-of-sight column density, photon index, scatter fraction (fscat), inclination angle, χ^2/dof , and the intrinsic 2-10 keV flux and luminosity. f means the value is fixed during the fitting. u means the scatter factor reaches the upper limit.

Name	ObsID	Cross constant CTKcover	$N_{\text{H,los}} [10^{22} \text{ cm}^{-2}]$ fscat	Γ $\chi^2_r (\chi^2/\text{dof})$	Norm [photons/keV/cm ² /s] $\log f_{\text{int},2-10\text{keV}}$	Inclination angle $\log L_{\text{int},2-10\text{keV}}$	torsigma
ESO362-G18	60201046002	0.980±0.008 0.25 ± 0.02	0.02±0.00 0.00 ^u	1.56 ± 0.00 1.13(3094/2737)	2.43e-03 ± 5.70e-04 -10.916 ± 0.102	73 ± 6 42.621 ± 0.102	13 ± 1
NGC1365	60002046002	1.020±0.013 0.28 ± 0.01	12.45±1.50 0.05 ^u	1.61 ± 0.05 1.11(384/346)	4.64e-03 ± 3.41e-04 -10.665 ± 0.047	70 ± 9 42.161 ± 0.047	84 ± -1
NGC1365	60002046003	1.010±0.011 0.28 ± 0.01	12.08±0.77 0.05 ^u	1.53 ± 0.01 1.21(473/391)	3.63e-03 ± 2.07e-04 -10.716 ± 0.026	70 ± 9 42.110 ± 0.026	2 ± 1
NGC1365	60702058002	1.030±0.013 0.28 ± 0.01	15.06±1.59 0.05 ^u	1.45 ± 0.05 1.23(474/387)	2.51e-03 ± 2.11e-04 -10.821 ± 0.051	70 ± 9 42.005 ± 0.051	84 ± 68
NGC1365	60702058004	1.030±0.015 0.28 ± 0.01	17.12±1.95 0.05 ^u	1.50 ± 0.04 1.19(350/293)	3.07e-03 ± 2.37e-04 -10.768 ± 0.044	70 ± 9 42.058 ± 0.044	84 ± 74
NGC1365	60702058006	1.020±0.031 0.28 ± 0.01	25.72±4.49 0.05 ^u	1.37 ± 0.05 1.17(99/85)	2.16e-03 ± 2.81e-04 -10.829 ± 0.067	70 ± 9 41.997 ± 0.067	84 ± -1
NGC1365	60702058008	1.040±0.014 0.28 ± 0.01	11.80±1.36 0.05 ^u	1.54 ± 0.04 1.21(420/347)	3.20e-03 ± 2.26e-04 -10.778 ± 0.041	70 ± 9 42.048 ± 0.041	84 ± -1
NGC1365	60702058010	1.050±0.015 0.28 ± 0.01	23.13±2.03 0.05 ^u	1.40 ± 0.03 1.28(387/302)	2.40e-03 ± 1.67e-04 -10.805 ± 0.037	70 ± 9 42.021 ± 0.037	84 ± 56
NGC1365	60702058012	1.000±0.017 0.28 ± 0.01	99.83±4.02 0.05±0.01	1.60 ± 0.04 1.17(314/269)	7.49e-03 ± 1.36e-03 -10.450 ± 0.084	70 ± 9 42.376 ± 0.084	0 ± 5
NGC4151	60001111002	0.979±0.004 0.30 ± 0.00	6.19±0.72 0.05 ^u	1.72 ± 0.01 1.35(1011/748)	8.89e-02 ± 6.16e-03 -9.456 ± 0.031	78 ± 1 42.924 ± 0.031	21 ± 3
NGC4151	60001111003	0.997±0.002 0.30 ± 0.00	7.76±0.06 0.03±0.01	1.60 ± 0.00 1.63(1610/987)	7.56e-02 ± 1.25e-03 -9.445 ± 0.007	78 ± 1 42.936 ± 0.007	4 ± 0
NGC4151	60001111005	1.000±0.002 0.30 ± 0.00	7.38±0.28 0.05 ^u	1.72 ± 0.01 1.73(1761/1018)	9.79e-02 ± 1.41e-03 -9.414 ± 0.009	78 ± 1 42.966 ± 0.009	25 ± 1
NGC4151	60502017002	0.988±0.003 0.30 ± 0.00	9.19±0.47 0.05 ^u	1.75 ± 0.01 1.39(1135/819)	9.68e-02 ± 2.25e-03 -9.440 ± 0.012	78 ± 1 42.941 ± 0.012	27 ± 1
NGC4151	60502017004	0.999±0.002 0.30 ± 0.00	6.05±0.42 0.05 ^u	1.76 ± 0.01 1.27(1192/938)	1.19e-01 ± 5.48e-03 -9.357 ± 0.021	78 ± 1 43.024 ± 0.021	22 ± 2
NGC4151	60502017006	0.995±0.003 0.30 ± 0.00	4.49±0.18 0.05±0.05	1.69 ± 0.01 1.44(1198/833)	9.19e-02 ± 2.52e-03 -9.422 ± 0.014	78 ± 1 42.959 ± 0.014	7 ± 0
NGC4151	60502017008	0.985±0.003 0.30 ± 0.00	8.24±0.50 0.05 ^u	1.74 ± 0.01 1.41(1103/785)	8.62e-02 ± 2.49e-03 -9.483 ± 0.014	78 ± 1 42.897 ± 0.014	38 ± 10
NGC4151	60502017010	0.976±0.003 0.30 ± 0.00	7.52±0.45 0.05 ^u	1.73 ± 0.01 1.43(1127/788)	8.68e-02 ± 2.03e-03 -9.474 ± 0.012	78 ± 1 42.907 ± 0.012	24 ± 2
NGC4151	60502017012	0.978±0.004 0.30 ± 0.00	6.70±0.49 0.05 ^u	1.75 ± 0.01 1.28(997/780)	8.96e-02 ± 5.68e-03 -9.473 ± 0.028	78 ± 1 42.907 ± 0.028	46 ± 16
NGC5548	60002044002	1.000±0.008 0.00 ± -1.00	2.51±0.17 0.05 ^u	1.76 ± 0.01 1.00(427/428)	1.84e-02 ± 5.41e-03 -10.178 ± 0.128	38 ± 26 43.645 ± 0.128	19 ± 5
NGC5548	60002044003	1.010±0.008 0.00 ± -1.00	1.93±0.24 0.05 ^u	1.78 ± 0.02 1.00(415/416)	1.55e-02 ± 2.42e-03 -10.266 ± 0.069	38 ± 26 43.557 ± 0.069	26 ± 1
NGC5548	60002044005	0.985±0.006 0.00 ± -1.00	3.56±0.52 0.05 ^u	1.74 ± 0.02 0.96(520/540)	1.61e-02 ± 4.69e-03 -10.222 ± 0.127	38 ± 26 43.601 ± 0.127	20 ± 5
NGC5548	60002044006	1.020±0.006 0.00 ± -1.00	1.66±0.23 0.05 ^u	1.80 ± 0.02 1.07(575/539)	1.67e-02 ± 1.46e-03 -10.247 ± 0.040	38 ± 26 43.576 ± 0.040	73 ± 72
NGC5548	60002044008	0.977±0.007 0.00 ± -1.00	3.91±0.40 0.05 ^u	1.73 ± 0.03 0.95(510/535)	1.24e-02 ± 9.45e-04 -10.329 ± 0.039	38 ± 26 43.494 ± 0.039	27 ± 10
NGC5548	90701601002	1.010±0.008 0.00 ± -1.00	1.84±0.24 0.05 ^u	1.78 ± 0.02 0.94(447/474)	1.40e-02 ± 1.37e-03 -10.310 ± 0.045	38 ± 26 43.513 ± 0.045	84 ± -1
NGC7582	60061318002	0.967±0.021 0.30 ± 0.07	19.25±3.24 0.05 ^u	1.40 ± 0.06 1.25(188/151)	2.49e-03 ± 2.70e-04 -10.789 ± 0.063	60 ± 13 42.005 ± 0.063	84 ± -1
NGC7582	60061318004	0.981±0.026 0.30 ± 0.07	41.95±5.67 0.05 ^u	1.47 ± 0.09 1.40(158/113)	3.13e-03 ± 8.11e-04 -10.739 ± 0.129	60 ± 13 42.055 ± 0.129	84 ± -1
NGC7582	60201003002	0.990±0.009 0.30 ± 0.07	24.15±1.38 0.05±0.03	1.61 ± 0.04 1.09(537/491)	8.79e-03 ± 8.23e-04 -10.388 ± 0.049	60 ± 13 42.406 ± 0.049	23 ± 7

Table B4. Part of *NuSTAR* data analysis results for the five CLAGNs from the literature. The table lists the source name, observational ID, instrument, the model to fit the spectra, column density from the line of sight, the photon index, X-ray luminosity, and references.

Name	ObsID	Instrument	model	$N_{\text{H},\text{los}}$	Γ	$\log L_{\text{X-ray}}$	Reference
ESO362-G18	0790810101/60201046002	XMM-Newton/NuSTAR	double warm corona	0.66±0.10	1.66±0.03	42.59	Zhong & Wang (2022)
NGC1365	0692840301/60002046005	XMM-Newton/NuSTAR	pha*gabs1*gabs2(pow+laor)	7.54 ^{+0.5} ₋₀	2.09±0.05	42.40	Liu et al. (2021)
NGC1365	0692840401/60002046007	XMM-Newton/NuSTAR	pha*gabs1*gabs2(pow+laor)	4.16 ^{+0.4} ₋₀	2.10±0.05	42.35	Liu et al. (2021)
NGC1365	0692840501/60002046009	XMM-Newton/NuSTAR	pha*gabs1*gabs2(pow+laor)	12.04 ^{+0.6} ₋₀	1.92±0.06	42.28	Liu et al. (2021)
NGC5548	60002044006	NuSTAR	tbabs*ztbabs(pexrav+zgauss)	4.46 ^{+2.1} ₋₂	1.79±0.09	43.49	Pal et al. (2022)
NGC5548	60002044005	NuSTAR	tbabs*ztbabs(pexrav+zgauss)	5.61 ^{+2.3} ₋₂	1.62±0.10	43.44	Pal et al. (2022)
NGC5548	60002044003	NuSTAR	tbabs*ztbabs(pexrav+zgauss)	4.77 ^{+1.3} ₋₂	1.81±0.08	43.37	Pal et al. (2022)
NGC5548	60002044002	NuSTAR	tbabs*ztbabs(pexrav+zgauss)	6.06 ^{+1.6} ₋₂	1.75±0.10	43.43	Pal et al. (2022)
NGC5548	60002044008	NuSTAR	tbabs*ztbabs(pexrav+zgauss)	6.91 ^{+2.5} ₋₂	1.61±0.11	43.35	Pal et al. (2022)
NGC5548	90701601002	NuSTAR	tbabs*ztbabs(pexrav+zgauss)	3.66 ^{+1.2} ₋₂	1.81±0.09	43.36	Pal et al. (2022)
NGC7582	60201003002	NuSTAR	tbabs(cutoffpl*TBpcf+xillver)	44.4 ^{+1.5} ₋₂	1.55±0.03	41.99	Lefkir et al. (2023)
NGC7582	60201003002	NuSTAR	tbabs(cutoffpl*TBpcf+xillver)	42.89±1.50	1.65±0.03	42.14	Lefkir et al. (2023)
NGC7582	60201003002	NuSTAR	tbabs(cutoffpl*TBpcf+xillver)	35.88±2.20	1.57±0.05	42.10	Lefkir et al. (2023)
NGC7582	60201003002	NuSTAR	tbabs(cutoffpl*TBpcf+xillver)	50.61 ^{+1.6} ₋₂	1.62±0.04	42.15	Lefkir et al. (2023)
NGC7582	60201003002	NuSTAR	tbabs(cutoffpl*TBpcf+xillver)	55.11 ^{+3.0} ₋₉	1.57±0.05	41.87	Lefkir et al. (2023)
NGC7582	60061318004	NuSTAR	tbabs(cutoffpl*TBpcf+xillver)	62.82 ^{+11.2} ₋₉	1.33±0.06	41.54	Lefkir et al. (2023)
NGC7582	60061318002	NuSTAR	tbabs(cutoffpl*TBpcf+xillver)	32.36 ^{+4.6} ₋₉	1.38±0.05	41.63	Lefkir et al. (2023)
NGC7582	60201003002	NuSTAR	tbabs(cutoffpl*TBpcf+xillver)	43.57 ^{+3.0} ₋₂	1.50±0.04	41.90	Lefkir et al. (2023)
NGC7582	60201003002	NuSTAR	tbabs(cutoffpl*TBpcf+xillver)	45.84±1.60	1.51±0.04	42.02	Lefkir et al. (2023)